Journal of
Manufacturing and Materials Processing

MDPI

Article

LPBF-Produced Elastomeric Lattice Structures for Personal Protection Equipment: Mechanical Performance Versus Comfort-Related Attributes

William Turnier Trottier [1], Antoine Collin [1], Thierry Krick [2] and Vladimir Brailovski [1,*]

[1] Department of Mechanical Engineering, École de Technologie Supérieure, 1100 Notre-Dame Street West, Montreal, QC H3C 1K3, Canada; william.turnier-trottier.1@etsmtl.net (W.T.T.); antoine.collin.3@ens.etsmtl.ca (A.C.)
[2] Bauer Hockey LTD., 60, Jean-Paul Cayer Street, Blainville, QC J7C 0N9, Canada; thierry.krick@bauer.com
* Correspondence: vladimir.brailovski@etsmtl.ca; Tel.: +1-514-396-8594

Abstract: This study focuses on the energy absorption and wearer comfort attributes of regular lattice structures fabricated by laser powder bed fusion from two elastomeric materials, namely TPU1301 and TPE300, for use in personal protective equipment (PPE). This study compares Body-Centered Cubic (BCC), Face-Centered Cubic (FCC) and Kelvin (KE) lattice structures with density varying from 0.15 to 0.25 g/cm^3, cell size varying from 10 to 14 mm and feature size varying from 1 to 3 mm. Quasi-static and dynamic compression testing confirmed that among the studied geometries, KE structures printed with TPE300 powders provide the best combination of reduced peak acceleration and increased compliance, thereby improving both safety and comfort. Using the protection–comfort maps built on the basis of this study enables the design of lightweight and compact protective structures. For example, if a safety layer protecting a 100 mm^2 surface area can be manufactured from either TPE300 or TPU1100 powders using either KE or FCC structures, the KE TPE300 layer will be 1.5 times thinner and 2.5 times lighter than its FCC TPU1301 equivalent. The results of this study thus provide a basis for the optimization of lattice structures in 3D-printed PPE to meet both service and manufacturing requirements.

Keywords: additive manufacturing; laser powder bed fusion; lattice structures; TPU; thermoplastic elastomers; impact absorption

Academic Editor: Panagiotis Stavropoulos

Received: 31 March 2025
Revised: 2 May 2025
Accepted: 14 May 2025
Published: 29 May 2025

Citation: Turnier Trottier, W.; Collin, A.; Krick, T.; Brailovski, V. LPBF-Produced Elastomeric Lattice Structures for Personal Protection Equipment: Mechanical Performance Versus Comfort-Related Attributes. *J. Manuf. Mater. Process.* **2025**, *9*, 182. https://doi.org/10.3390/jmmp9060182

1. Introduction

Recent years have witnessed significant advancements in the development of advanced personal protective equipment (PPE), driven by the imperative to mitigate injuries from high-impact collisions. Risks associated with high-impact collisions have heightened the need for gear that not only mitigates injuries but also adapts to various loading conditions. One promising avenue in this regard involves the application of lattice structures, which offer unique mechanical properties that can be tailored to absorb energy and withstand repetitive stresses effectively [1]. These intricate architectures offer the potential to surpass conventional foam-based PPE by enabling localized customization and improved overall performance.

Thermoplastic polyurethane elastomers (TPUs) belong to the broader thermoplastic elastomer (TPE) family of materials, which soften reversibly when heated and harden when cooled [2], allowing the material to flow. These materials can be fabricated using conventional thermoplastic transformation processes [3] and consist of linear primary polymer chains composed of three basic building blocks: polyol (flexible), diisocyanate

(rigid) and a chain extender (flexible or rigid) [4]. The proportion of soft segments impacts the elastomeric and viscoelastic behavior of the polymer [4,5]. The proportion of hard segments, for its part, determines the hardness, elastic modulus, strength and upper use temperature of the polymer [6–8]. This tunability and flexibility, augmented with durability, make TPUs ideal candidates for impact-absorbing applications, including PPE, provided the latter are designed considering the TPUs' temperature–strain rate sensitivity [4,9,10].

Additive manufacturing (AM) technologies, particularly laser powder bed fusion (LPBF), enable unprecedented design freedom in fabricating complex geometries, including architectured materials, such as lattice structures. When compared to metal LPBF, polymer LPBF offers even greater flexibility by having the powder bed supporting the part being printed, thus eliminating the need for support structures [11]. While polymer LPBF has been extensively applied for polyamides [12,13], application of this technology to other polymers, such as TPUs, remains at an early stage of development [14–19].

As defined by Ashby and Gibson [1], cellular solids are composed of an interconnected network of solid struts or plates that form the edges and faces of cells. Their special arrangement can be in two dimensions (honeycombs) or three dimensions (foams or lattices) [20]. The present study is focused on tri-dimensional structures constructed using mesoscale unit cells that are repeated in 3D space. The pattern repetition of these structures can be realized stochastically or periodically, using either open or closed unit cells [1]. The porous nature of cellular structures confers them a higher specific strength and stiffness that what is obtained in dense materials [21]. Three main factors impact the properties of a lattice structure, regardless of the type of a unit cell involved [1,22]: (a) the bulk properties of the materials with which the lattice structure is made; (b) the shape, size and topology of the unit cell; (c) the relative density of the unit cell. Moreover, because of their strain-rate sensitivity [23,24], the stiffness of polymeric architectured materials, including foams and lattice structures, depends on whether they are used for static or dynamic applications [25,26].

A foam is a bulk cellular material characterized by a random, often isotropic distribution of cells within a continuous matrix, typically produced by chemical or physical foaming processes [27]. These structures naturally offer high energy absorption and cushioning properties. Tuning of their mechanical behavior is significantly limited and generally requires the selection of bulk material, cell structure and relative density [28]. These foams generally come in sheet form to be cut to specifications, or, in some instances, molding can be considered for complex parts.

Better suited for AM, periodic (non-stochastic) lattice structures are more easily tunable for a specific application than their stochastic counterparts [29], and they are generally classified as truss-based and sheet-based. In addition to a constitutive material, the density, the cell size and the unit cell topology are three codependent parameters that dictate the mechanical properties of lattice structures [1,30]. In the case of LPBF, only open unit cell lattices can be printed as there is a need for powder evacuation after fabrication. In keeping with the viscoelastic behavior of bulk TPUs, the mechanical behavior of lattice structures made of these materials is also strain rate-dependent [31]. While publications on lattice structures have grown substantially in recent years [32], research works on polymer LPBF lattices are very scarce when compared to their metallic equivalents. Among the available studies on polymeric lattice structures, nylon printed ones [30,33–38] are usually much better covered than their elastomeric counterparts [39–41].

The scientific literature presents several indicators for use in rating the quasi-static and dynamic performances of lattice structures for energy absorption in PPE. Whilst the protection aspects of PPE are generally well covered, their comfort is largely overlooked, thus potentially discouraging their active use and hampering the full protection of some

users [42]. Moreover, comfort evaluations frequently use qualitative indices and are highly sensitive to a responsiveness bias caused by product aesthetics [43]. Among the measurable indices employed for the comfort evaluation of foams used in PPE, four have been found to play a significant role in user perception [25,26,44,45]: (a) the initial compliance (inverse of firmness); (b) the bottoming-out prevention capacity; (c) the pressure redistribution capacity and (d) the heat redistribution capacity.

The following gaps related to 3D-printed elastomeric lattice structures designed for the use in PPE were identified. For instance, no works have been found on the dynamic response of lattice liners of different thicknesses with the same unit cell configuration in application cases relevant for PPEs. Moreover, no studies have thus far combined energy absorption performance with a quantitative comfort assessment. Additionally, the current literature often focuses on quasi-static testing, with limited attempts to correlate dynamically. Finally, no existing work has compared the PPE-related performances of different LPBF-printed lattice structures made of different elastomeric materials.

The main objective of this study is therefore to assess the static and dynamic energy absorption and comfort-related attributes of a series of polymer LPBF-printed regular open-cell lattice structures for use in PPE. This study starts by selecting the most appropriate elastomeric materials for 3D-printed lattice structures. Next, the structures that are most suitable for use in PPE are selected, designed, 3D-printed and experimentally tested in terms of their quasi-static and dynamic mechanical behavior in compression. They are then rated in terms of their suitability for use in PPE via the experimentally obtained energy absorption and comfort-related attributes. This leads to the introduction of a protection–comfort map of the tested configurations. Finally, as an example, the main geometric characteristics of some of the selected lattice structures are combined with their service performance to aid in the design of protective, comfortable, lightweight and compact PPE.

2. Materials and Methods

2.1. Materials

Two TPU materials were used to produce test samples for this study. The first is the thermoplastic elastomer TPE300 supplied by ALM (Advanced Laser Materials, Temple, TX, USA). This material is one of the first elastomers offered within the EOS Digital Foam methodology of producing "foam-like" products with 3D printing (EOS, Electro Optical Systems, Krailling, Germany). It is used to manufacture flexible parts with a 92 ShoreA hardness and an elongation at break of up to ~270% (Table 1). The second material is the thermoplastic polyurethane TPU1301 supplied by EOS with an ShoreA hardness 86 and an elongation at break of up to 250% (Table 1). The latter is the first flexible material being used in all EOS plastic line printers. EOS recommends using both materials to print seals, gaskets or lattice replacements of traditional foams in footwear and PPE. These two elastomers were selected for this study because of the availability of printing parameter sets for these materials. Moreover, both materials were developed with the objective of fulfilling functional requirements for flexible and shock-absorbing materials and structures and are therefore suitable for PPE-related applications.

Since the size and shape, as well as the thermal, physical and flow characteristics of the TPE300 and TPU1301 powders directly influence the process productivity and properties of the manufactured parts, both feedstock powders are analyzed in their "Ready to print" state.

Table 1. Typical bulk powder and printed part properties for TPE300 and TPU1301 elastomers (taken from EOS GmbH [46] and ALM [47]); XY and Z correspond, respectively, to the directions parallel and perpendicular to the building plate.

	Name	Unit	TPE300	TPU1301
Powder property	Bulk density	g/cm^3	0.60	0.49
	D10	µm	20	~22
	D50	µm	50	~72
	D90	µm	105	~138
Part property	Part density	g/cm^3	1.20	1.11
	Hardness	Shore A	92	86
	Tensile strength	MPa	XY: 20; Z: 15	XY: 7; Z: 5
	Elongation	%	XY: 267; Z: 180	XY: 250; Z: 90

2.2. Powder Characterization

2.2.1. Particle Size Distribution and Morphology

Following gold sputtering, powder particles were observed at different magnifications using a TM3000 Table-Top SEM (Hitachi High-Technologies Corporation, Tokyo, Japan). The particle size distribution (PSD) was measured using an LS 13 320 XR particle size analyzer (Beckham Coulter Inc., Brea, CA, USA) equipped with a Universal Liquid Module. For these measurements, each powder lot was tested 5 times, and for each test, about 50 mg of powder was scaled and mixed with distilled water and 5 drops of Tween 20 surfactant (Sigma-Aldrich, St-Louis, MO, USA).

2.2.2. Thermal Properties

To detect the temperatures at which the polymers begin to decompose, a PerkinElmer Pyris Diamond TGA (PerkinElmer, Waltham, MA, USA) was used (ASTM E1131-20 [48]). The degradation temperature was determined when the tested sample lost 1% of its original mass. The following protocol was applied in a UHP nitrogen (purged @ 100 mL/min) atmosphere: isothermal at 20 °C for 1 min followed by heating to 600 °C (10 °C/min rate) and isothermal for 2 min. To determine the process temperature window, a TA Instruments DSC 2500 (TA Instruments, New Castle, DE, USA) was used (ASTM D3418-21 [49]). Two sequential heating and cooling cycles (10 °C/min rate) were carried out in a UHP nitrogen (purged @ 50mL/min) atmosphere: isothermal at −50 °C for 5 min, followed by heating to 220 °C, isothermal for 5 min and cooling to −50 °C.

2.2.3. Flow Properties

An FT4 rheometer (Freeman Technology, Tewkesbury, UK) was used for measuring both the static and dynamic bulk powder properties. Among the obtained, the Coefficient of Bulk Density (CBD, kg/m^3) represents a good approximation of the density of a powder bed in a 3D printer. In addition to the CBD, five tests were performed with the FT4 to compare the flow properties of powders used in this study: (a) aeration, to rate powders based on their sensitivity to aeration and cohesion; (b) permeability, to provide a comparative index of the cohesion, size, shape and distribution of powder particles; (c) compressibility, to evaluate the powder behavior during compaction; (d) shear resistance, to assess the ease with which a powder at rest can flow; and (e) stability and dynamic flow, to measure the sensitivity of a powder flow to flow rate and to evaluate the powder cohesion.

2.3. Printing and Post-Processing

TPE 300 was printed on an EOS P770 printer using a 120 µm layer thickness. The exposure parameter set consisted of 6 contour exposures with an alternating hatching. For this study, a new batch of powder was preconditioned to minimize the effect of powder

aging on printing results [11]. The powder batch prepared was sufficiently large so all of the samples of this study were printed without the need for powder refresh or reuse.

TPU1301 was printed on an EOS Formiga P110 Velocis SLS at a 100 µm layer thickness using the "structure_mechanic" exposure parameter set. This set consisted of 6 contour exposures with an alternating hatching recommended for fine lattice structures (strut thickness $\leq$ 2mm) with high mechanical requirements [50]. With the P110 build volume being ~1/10 of P770, it was not feasible to prepare the total powder volume required for the study without creating handling issues. Consequently, the powder was reused with a refresh factor of 20% new powder to maintain the apparent bulk density > 0.4g/cm^3, with the latter measured using an ASTM D1895-17 Method A funnel [51]. This was deemed necessary to mitigate powder degradation potentially affecting the surface finish and mechanical properties of printed parts [50].

Part Positioning and Orientation

For printing, the part positioning was realized using Magics 25.04 software (Materialise NV, Leuven, Belgium). For this study, all the lattice structures were printed with a 45° angle with respect to the XY plane. This was performed to avoid positioning large flat areas horizontally, which can generate part curling due to uneven shrinkage of the part [52,53]. Moreover, printing at this angle was intended to mitigate and average out the anisotropy typically induced by the LPBF process, where properties can vary significantly as a function of the build direction [54–56]. Despite this precaution, it is acknowledged that anisotropy could still affect the mechanical performance of the structures.

Once positioned, the slices of each build volume were created using the RP-Tools 6.2 add-on (EOS GmbH, Krailling, Germany). The building parameters were prepared using EOS PSW 3.6 software (EOS GmbH, Krailling, Germany) and sent out to the machine for printing. For post-processing, the parts were manually removed from the part cake and cleaned using compressed air. Final cleaning was carried out using a DyeMansion Powershot C system (DyeMansion GmbH, Planegg, Germany) with a Polyshot PC4 plastic-based blasting medium.

2.4. Bulk Printed Material Testing

The bulk material hardness was measured in accordance with the ASTM D2240-15 standard [57] using an MS-1 Multi Scale Dial Durometer (Rex Gauge LLC, Buffalo Grove, IL, USA) with a Shore D barrel installed. Before and after the tests, the durometer was calibrated using Shore A calibration blocks (TBK-A, Rex Gauge LLC, Buffalo Grove, IL, USA). For these measurements, 42 mm diameter, 7 mm thick flat samples were printed parallel to the building plate (Figure 1). For each material, the hardness was taken 10 times, and each measurement was distanced at least 6 mm from the previous ones and 12 mm from the sample edges. The bulk tensile properties were measured using an Alliance RF/200 Electromechanical Universal Testing Machine (MTS Systems Corporation, Eden Prairie, MN, USA). The testing was performed using a 10 kN load cell with flat-faced pneumatic grips at a 50 mm/min strain rate until failure, following the ASTM D638-14 standard [58]. Due to large elongations expected from the tested materials, Type IV test specimens with a nominal thickness of 4 mm (Figure 1) were used in conjunction with a DX2000 High Strain Extensometer (MTS Systems Corporation, Eden Prairie, MN, USA). The tensile testing routine was repeated for three build orientations (XY, 45 and Z), and ten samples of each material were tested.

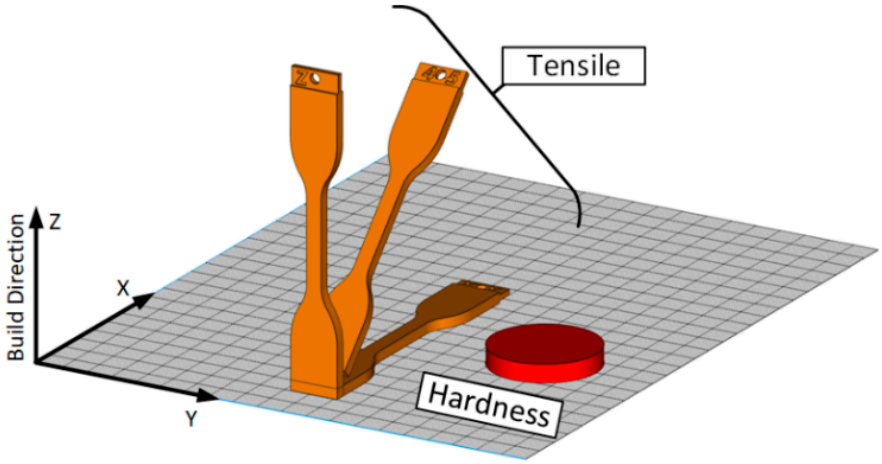

Figure 1. Printing orientations for hardness and tensile testing samples.

2.5. Lattice Structures

2.5.1. Principles of Lattice Selection

This study focuses on non-stochastic (periodic) structures, which are easier to design and control than their stochastic (random) counterparts [29]. The need to remove powder from the pores of printed structures limited this study to examining open-cell structures. Based on the above considerations, 5 truss-based and 3 triply periodic minimal surface (TPMS) cell designs were initially considered: Simple Cubic (SC), Kelvin (KE), Face-Centered Cubic (FC), Body-Centered Cubic (BC), Re-Entrant (RE), Gyroid (GY), Schwarz-D (SD) and Schwarz-P (SP) (nTop software, nTopology 4.21.2, Inc. New York, NY, USA). Among the truss-based lattices, SC structures present the highest strain sensitivity and anisotropy [59], which is not adequate for PPE, where impacts are multi-directional. Among the TPMS lattices, SP structures exhibit a greater anisotropy than the other TPMS structures [60], thus also making SP less well suited for applications requiring high stiffness and strength in multiple directions [35]. For the above reasons, the SC and SP lattice structures were discarded, while the following six structures were retained for further analysis (Figure 2): Kelvin (KE), Face-Centered Cubic (FC), Body-Centered Cubic (BC), Re-Entrant (RE), Gyroid (GY) and Schwarz-D (SD).

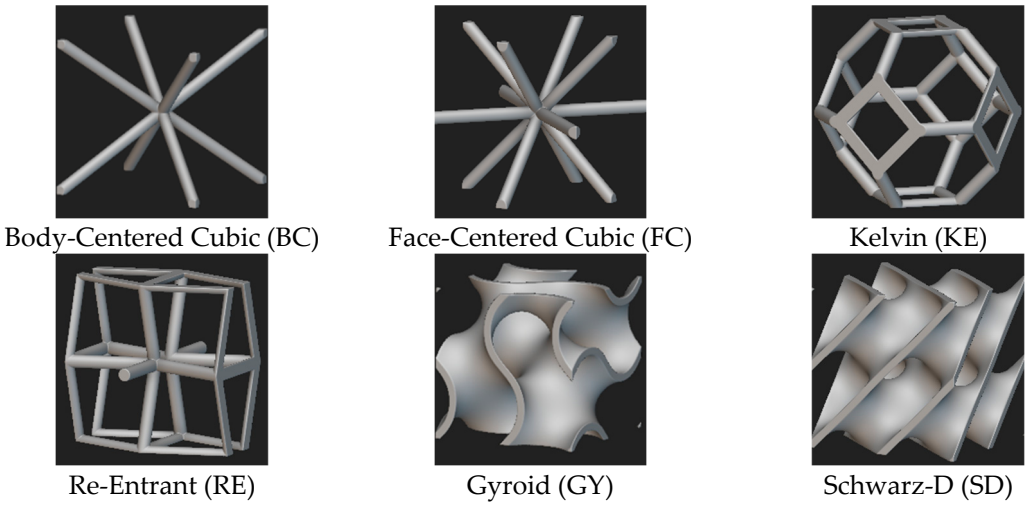

Figure 2. Unit cells of the six lattice structures selected for the study.

Three codependent geometric parameters of the lattice structures were considered for the study: the feature size (strut or sheet thickness), the cell size and the relative density

of a cell. The cell size and the relative density of the lattices were considered as driving parameters, and the feature size was considered as a dependent parameter.

- Feature size (strut or wall thickness): EOS GmbH suggests printing with feature sizes varying between 1 and 3 mm [50]. The minimum feature size is constrained mainly by the laser spot size and the powder particle size distribution [61,62]. It also corresponds to the equivalent of 6 contours of the "structure_mechanic" parameter set, considering the effective spot size of a CO_2 laser being equal to ~50 µm [63]. For its part, the maximum recommended feature size of 3 mm does not have a clear indication in the literature or application notes. With these limits in mind, it is possible to determine the minimum achievable densities of lattice structures while still ensuring their satisfactory manufacturability.
- Cell size: Setting the proper cell size is crucial to meeting functional requirements without compromising manufacturability. The minimum cell size is commonly determined by the need for powder removal. This is why printing lattice structures with a cell size smaller than 5 × 5 × 5 (mm) is not recommended [50]. In the present study, preliminary printing of lattices with a cell size between 5 × 5 × 5 and 10 × 10 × 10 (mm) revealed the need for an extra manual operation to remove the powder, in addition to automatic de-powdering. In the case of industrial applications, additional cleaning would greatly slow down the manufacturing process, and the remaining particles would affect the process repeatability and pose risks to user health and safety. This is why the smallest cell size of this study was set to 10 × 10 × 10 (mm). Furthermore, from the open literature, it was found that the thickness of most compact protective liners corresponds to 15–20 mm [34,64,65]. This further highlights the importance of providing the greatest number of unit cells within a limited volume to achieve the highest possible protection levels [30,66]. The largest cell size of this study had to be determined by the need to keep at least one complete unit cell within a PPE to mitigate the effects caused by incomplete unit cells while conforming to complex shapes of protective liners [67]. Considering the above, the largest cell size was set to 14 × 14 × 14 (mm).
- Density: The upper density limit of this study was set to 0.25 g/cm^3. Higher densities were not considered as they fall outside the scope of the high-performance low-density viscoelastic foams used in PPE [68]. After preliminary fabrication tests, it was found that structures with a relative density of 0.10 g/cm^3, even respecting the minimum feature size requirements [50], were very fragile. Moreover, these structures had very low energy absorption capacities, augmenting the risk of damaging the dynamic testing equipment. Consequently, the lower density limit was set to 0.15 g/cm^3.

These parameters were specifically chosen to ensure that the lattice structures could emulate the properties of polymer foams commonly used in PPE. It can be observed in Figure 3 that the function that relates the relative density with the cell size/feature size ratio follows a power law and allows to calculate the feature size of a selected lattice structure of a given density and with a known cell size. For example, to reach a density of 0.15 g/cm^3 (lower limit of this study) in the BC structures using the smallest cell size of 10 × 10 × 10 (mm), the cell size/feature size ratio must be equal to 6.0, which requires a feature size of ~1.67 mm, which is within the recommended 1–3 mm range of printable features [50].

It can also be observed in Figure 3 that the Gyroid and Schwarz-D TPMS unit cells do not allow us to cover the entire density range established for this study (0.15–0.25 g/cm^3), while respecting the recommended printable feature size (1–3 mm). Both were therefore withdrawn from further consideration. To study the remaining four truss-based lattice

structures (Body-Centered Cubic (BC), Face-Centered Cubic (FC), Kelvin (KE) and Re-Entrant (RE)), this work was divided into three consecutives phases.

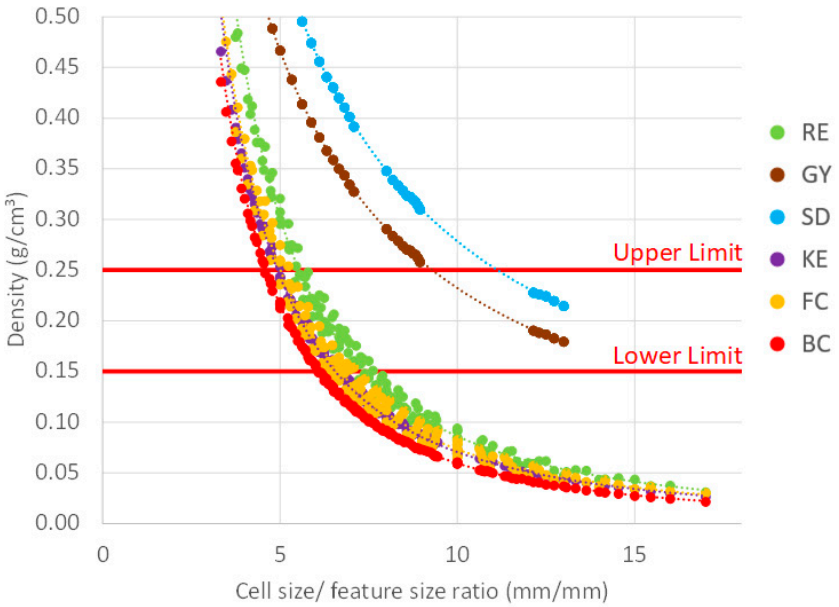

Figure 3. Relationship between the cell/feature size ratio and the relative density of the studied lattice cells.

2.5.2. First Phase (4 Lattice Structures): Varying Unit Cell Design

For the first phase of this study, the cell size was set to 10 × 10 × 10 (mm) and the relative density was set to 0.25 g/cm^3 (Figure 3). As seen in Table 2, for this cell size and density, the resulting feature size varied from 1.80 to 2.17 mm. After completion of this phase, four structures were compared in terms of their ability to meet the service-based performance criteria (introduced further), and two best structures (Lattice 1 and 2) were selected for the next phases of the study.

Table 2. Configurations studied in the first phase of the project (unit cell design).

Property	Unit				
Structure		BC	FC	KE	RE
Rel. Density	g/cm^3	0.25			
Cell size	mm	10 × 10 × 10			
Feature size	mm	2.17	1.99	2.03	1.80

2.5.3. Second Phase (2 Lattice Structures): Varying Relative Density

With the first phase of the study confined to the upper limit of the relative density, the objective of the second phase was to assess the performances of selected Lattices 1 and 2 with different relative densities: 0.15, 0.2 and 0.25 g/cm^3. In this case, the cell size remained at 10 × 10 × 10 (mm) with the feature size being a dependent parameter.

2.5.4. Third Phase (2 Lattice Structures): Varying Unit Cell Size

The same lattice structures as those in Phase 2 (Lattice 1 and 2) were used to focus on the impact of cell size variations at a fixed relative density, 0.25 g/cm^3 in this case. The cell sizes studied here were 10 × 10 × 10, 12 × 12 × 12 and 14 × 14 × 14 (mm). As in the preceding phases, the feature size was a dependent parameter for the given cell size and density combination.

2.6. Specimen Design and Testing Protocols

Considering the potential application of lattice structures in PPE, two complementary characterization modes were applied in compression: quasi-static and dynamic (impact).

2.6.1. Quasi-Static Testing

Geometric considerations for the design of compression test samples (Figure 4A) were drawn from ASTM DIS52959 [69]. For ductile materials, a minimum of 4 × 4 × 4 unit cells per sample must be used to mitigate the effects of the boundary conditions and accurately reflect the performance of a bulk lattice structure. Two endplates with a minimum thickness of 2 mm each were added to allow for a uniform distribution of the compressive loading on the tested lattice structure. According to ASTM D3574-17 [70], the samples must have a minimum surface area and thickness of 2500 mm^2 and 20 mm, respectively. The thickness of the samples should not be greater than 75% of the smallest dimension between the width and depth of the sample. Given these requirements, the quasi-static specimens had a lattice volume of 70 × 70 × 48 (mm), with the thickness representing around 70% of the top dimension and a surface area of 4900 mm^2. This configuration allowed us to test cell sizes up to 14 × 14 × 14 (mm). All configurations were tested three times with a new sample used each time. To provide a better understanding of the structure deformation occurring during testing, the third tested sample was filmed using an EOS 7D MkII camera (Canon Inc., Tokyo, Japan) with a Tamron SP 24-70 mm F2.8 lens (Tamron Co., Ltd., Saitama, Japan) attached.

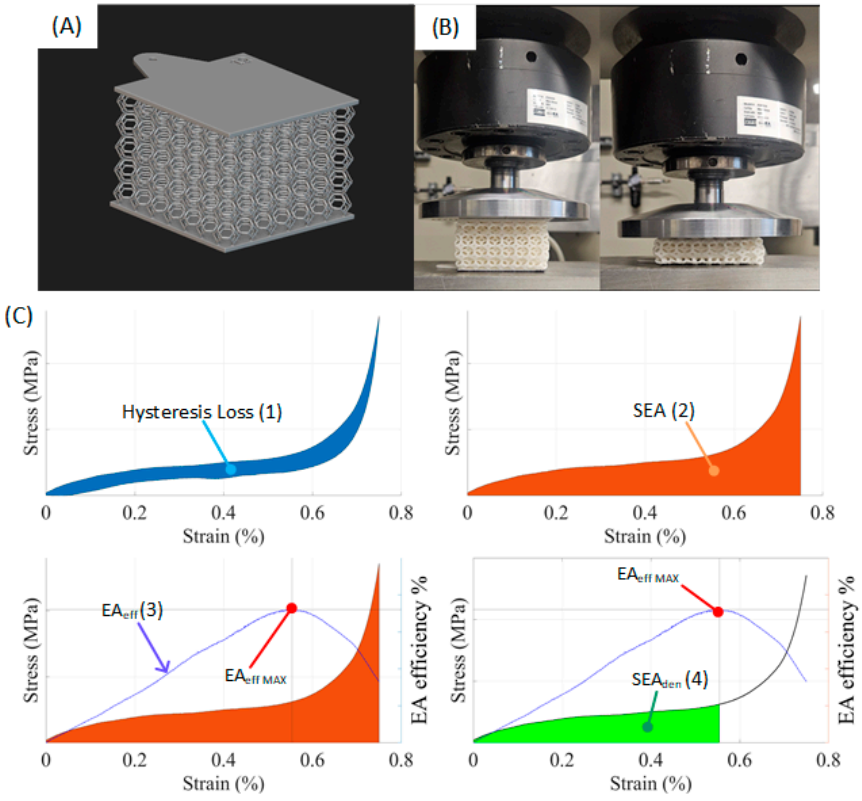

Figure 4. (**A**) Numerical model of a quasi-static testing sample and (**B**) structure during compression testing; (**C**) typical compression loading–unloading diagrams obtained during quasi-static loading–unloading testing with four energy absorption-related indicators.

Quasi-static compression tests were performed with an Alliance RF/200 Electromechanical Universal Testing Machine (MTS Systems Corporation, Eden Prairie, MN, USA) using a 10 kN or 200 kN load cell with a hardened steel compression tool and block

(Figure 4B). The load cells were swapped when lower-density specimens had to be tested. The test procedure followed ASTM D3574-17 [70], with the "N-test Procedure B" for hysteresis loss and a compression of 75%. Typical stress–strain loading–unloading diagrams are shown in Figure 4 with four different energy absorption indicators.

Two service-related quasi-static performance criteria were established for this study: the first was related to energy absorption and the second, to wearer comfort, when integrating these structures into PPE. The main objective of these quasi-static tests was to compare the energy absorption performance of lattice structures rather than providing values directly applicable to PPE.

Four indicators are commonly used to assess energy absorption during quasi-static testing: (a) hysteresis loss, (b) specific energy absorption (SEA), (c) energy absorption efficiency (EA_{eff}) and (d) specific energy absorption at densification (SEA_{den}).

The hysteresis loss (1) calculations were adapted from ASTM D2517-17. This indicator refers to the energy dissipation occurring in a material during one loading $\sigma_l(\varepsilon)$–unloading $\sigma_u(\varepsilon)$ cycle (see stress–strain diagram in Figure 4C). For PPE, the hysteresis loss (1) is generally considered to be a good indicator of the energy dissipated during impact [4] and is defined as the difference between the loading and unloading energies expressed as a percentage of the loading energy:

$$Hysteresis\ Loss = \frac{\int_0^{\varepsilon_{max}} \sigma_l(\varepsilon)d\varepsilon - \int_0^{\varepsilon_{max}} \sigma_u(\varepsilon)d\varepsilon}{\int_0^{\varepsilon_{max}} \sigma_l(\varepsilon)d\varepsilon} * 100\% \quad (1)$$

It is also possible to extract other indicators that could be used to define the energy absorption qualities of a structure. The next indicator is the specific energy absorption (SEA), which represents the energy absorbed (work) by a sample during loading divided by its mass (usually in J/g) [71,72]. To calculate SEA (2), the entire loading stress–strain diagram σ(ε) is integrated and divided by the relative density of a sample (ρ) (Figure 4C). This indicator is especially useful in applications where the mass is a limiting factor.

$$SEA = \frac{1}{\rho}\int_0^{\varepsilon_{max}} \sigma(\varepsilon)d\varepsilon \quad (2)$$

Derived from SEA, the energy absorption efficiency (EA_{eff}) (3) is defined by the ratio of absorbed energy to stress and is denoted as

$$EA_{eff} = \frac{1}{\sigma(\varepsilon)}\int_0^{\varepsilon_{max}} \sigma(\varepsilon)d\varepsilon \quad (3)$$

The maximum value of EA_{eff} corresponds to the inflection point of a stress plateau, i.e., to the onset of densification (ε_D), Figure 4C. If the loading stress–strain curve in (2) is integrated up to the onset of densification, SEA becomes SEA at densification (SEA_{den} (4)):

$$SEA_{den} = \frac{1}{\rho}\int_0^{\varepsilon_D} \sigma(\varepsilon)d\varepsilon \quad (4)$$

Traditionally, the Shore hardness is used to quantify the comfort level of foam-type materials. A lower Shore would correspond to a foam that has a higher wearer comfort level by offering a better pressure redistribution [25]. In the case of lattice structures, this measurement method would quantify the hardness of a bulk material and not of a lattice structure. Therefore, in this study, the Shore hardness was replaced by the reciprocal of the elastic modulus of a structure, i.e., by its compliance (in MPa^{-1}). The compliance should be maximized to improve wearer comfort.

2.6.2. Dynamic Testing (Impact)

For the design of PPE using elastomeric materials, it is imperative to perform dynamic testing to account for the strain-rate sensitivity of the material [4,9,10] and for the geometric non-linearities of lattice structures [73]. Since, in the present study, only lattice structures were tested, the results of dynamic tests do not provide definitive answers on their overall performance within PPE [64]. Dynamic samples (Figure 5A) were also designed with two 2 mm thick endplates as their quasi-static counterparts. The lattice impact area was 100 × 100 mm, to ensure proper coverage by a hemispherical impactor. All configurations were tested three times, with a new sample used each time. The testing protocol for dynamic tests went as follows: (A) Structures were tested at an ambient temperature of 20 ± 2 °C with the humidity not exceeding 55%. (B) Each lattice structure was tested at three thicknesses: 20, 30 and 40 mm. (C) Three impacts were made per sample, with the last impact being reported. (D) Each impact was made at an interval of 60 s from the prior impact. (E) The impact velocity was set to 4.5 m/s, which is slightly lower than the velocities commonly seen in open literature or standards for PPE tests (6–10 m/s) [64,65,74], since preliminary testing of thin samples showed the risk of damaging the testing equipment.

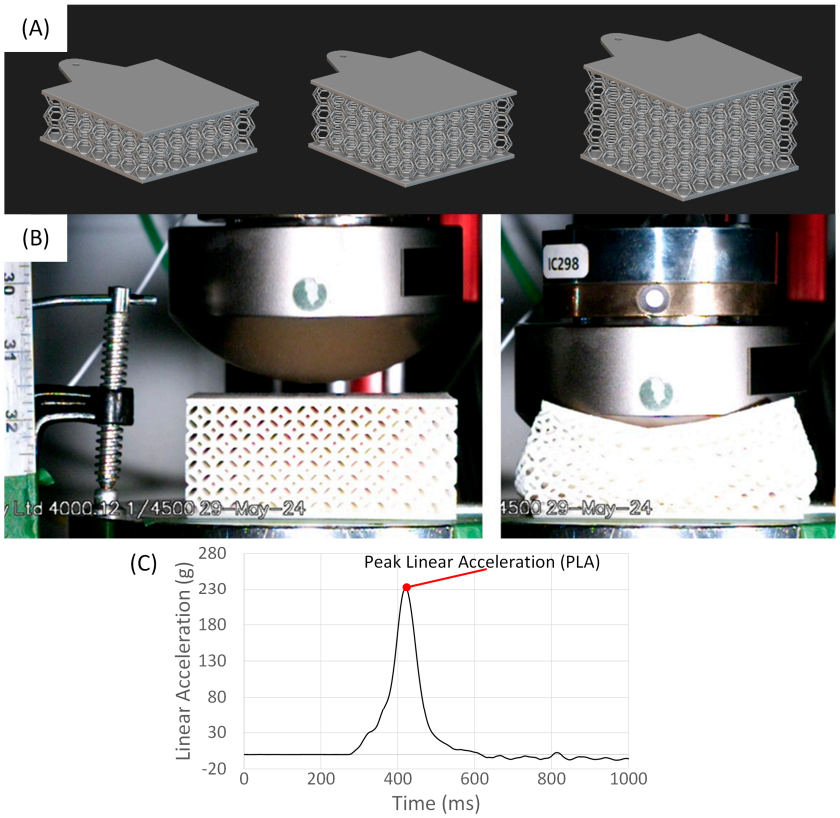

Figure 5. (**A**) Numerical model of a typical dynamic specimen and (**B**) structure during dynamic testing; (**C**) typical PLA diagram.

For dynamic testing, the peak linear acceleration (PLA) and the pulse length are the two main energy absorption indicators for dynamic tests. The lower the value of PLA and the longer the pulse length, the greater the user protection. In this work, PLA (Figure 5C) is considered as the direct target value for the protection level of an architecture structure, and it was measured by a uniaxial accelerometer installed inside the impactor of a Cadex monorail impact machine (Cadex Inc, Saint-Jean-Sur-Richelieu, QC, Canada). The mass of the carriage assembly was 5 kg, and it is representative of the mass of an average human head [75].

Before and after the testing, the system was verified using a 60 ± 5 Shore A flat modular elastomer programmer (MEP) that comes standard with the drop tower. Six impacts with a velocity of 5.2 m/s, measured on the last 40 mm of fall, at an interval of 75 s, were made, as stated by the equipment manufacturer. The PLAs of the last three impacts were recorded. To be valid, the means of the three post-test PLA values should not differ by more than 5% from the mean of pre-test PLA values. In a bid to protect the testing equipment, samples were tested with incrementally increasing accelerations, thereby going from the thickest to the thinnest. There was an accepted possibility that certain thicknesses would not be tested if the PLA value obtained with a thicker sample approached the machine acceleration limit. Like the quasi-static tests, the dynamic test was filmed using an Edgertronic SC2 high-speed camera (Sandstreak Corp., Campbell, CA, USA) with a Nikon 50 mm F1.8 lens (Nikon Corp., Shinagawa, Tokyo, Japan).

3. Results

3.1. Powder Characterization

3.1.1. Particle Size Distribution and Morphology

From the SEM micrographs shown in Figure 6A,B, both powders present a very irregular particle morphology as a result of the cryogenic grinding of TPU/TPE pellets [15]. On larger particles, smaller satellites are attached due to mechanical interlocking or incomplete grinding of the pellets.

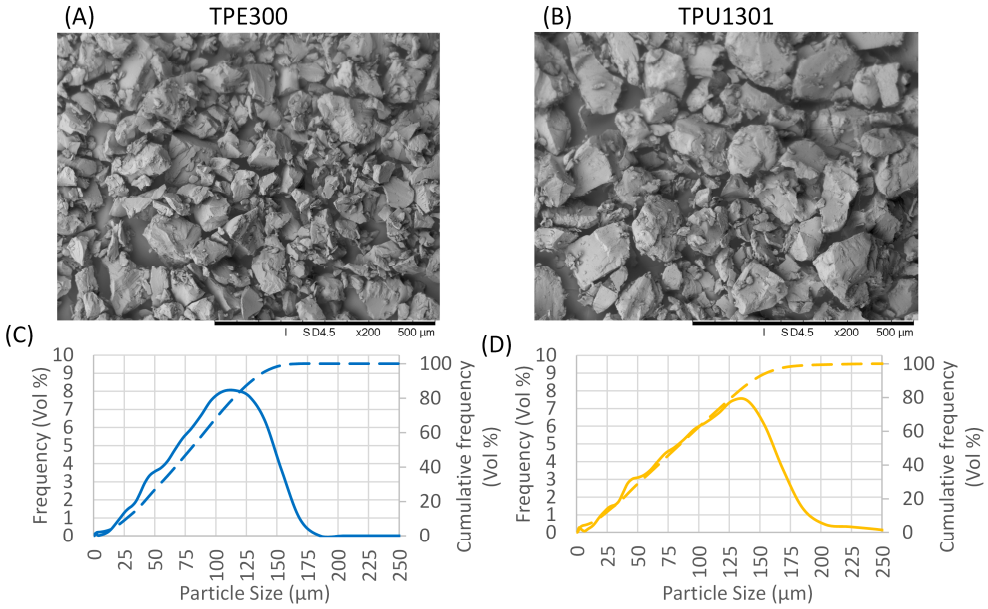

Figure 6. SEM micrographs: (**A**) TPE300 and (**B**) TPU1301 powders at 200× magnification and particle size distribution for (**C**) TPE300 and (**D**) TPU1301.

It can be seen from Figure 6C that TPE300 powder has a slightly narrower PSD and is, overall, finer than TPU1301 powder (Figure 6D). Moreover, it follows from Table A1 (Appendix A) that the D_{90} of both powders (135 µm for TPE300 and 150 µm for TPU1301) are greater than their respective layer thicknesses of 120 µm (TPE300) and 100 µm (TPU1301), meaning that during power spreading, some particles could be moved around the powder bed with the action of the recoating blade.

3.1.2. Thermal Properties

TGA analyses showed that the degradation temperatures of both powders are very close (1.3% difference): 280.8 °C for TPE300 and 284.6 °C for TPU1301. From the DSC

thermographs, however (Figure 7), it is obvious that the two materials have significantly different thermal responses. Both polymers present broad melting peaks with widths of 52 and 30 °C for TPE300 and TPU1301, respectively. These broad melting transitions, commonly seen in TPU, make it difficult to determine the powder bed temperature needed to prevent part caking [7,76]. Tabulated data can be found in Table A2 in Appendix A.

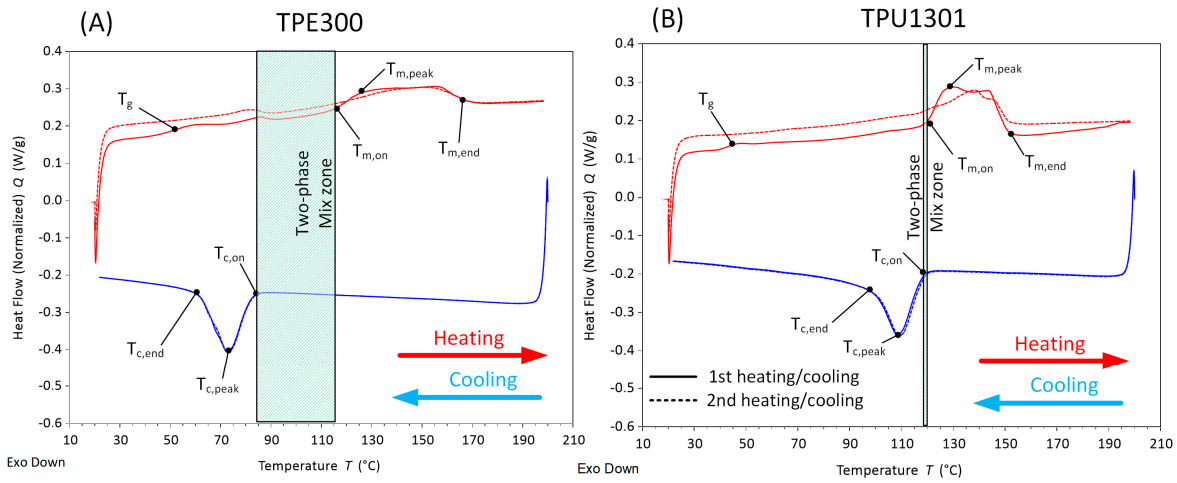

Figure 7. DSC thermograms: (**A**) TPE300 and (**B**) TPU1301.

For TPE300 (Figure 7A), the first change in the heating curve is at T_g and can be seen at around 50 °C. Thereafter, two endothermic peaks are observed at 85.5 and 134.5 °C, respectively, for the first heating cycle. The first peak can be attributed to the transition of soft segments of the elastomer, while the second peak represents the transition of hard segments [77]. Therefore, T_g would potentially belong to hard segments of the polymer. For the second heating, these peaks are seen at 81 and 149 °C, respectively. Looking at the second peak, the melting temperature range is very broad, going from an onset of 115 °C to an endset of 167.6 °C. The crystallization onset temperature of TPE300 is 82 °C, thus offering a broad operating temperature window (~30 °C). Contrary to TPE300, TPU1301 (Figure 7B) has a single clearly distinguishable endothermic peak with an onset at 120 °C and endset at 150 °C. The crystallization onset temperature of TPU1301 is 118 °C, making the operating temperature window of TPU1301 significantly narrower than that of TPE300 (~2 °C).

3.1.3. Flow Properties

Table 3 presents the rheological properties of both powders. In both cases, TPE300 presents a higher resistance to flow and a higher mechanical interlocking than TPU1301, as can be seen from the basic flow energy (BFE) and specific energy (SE) measurements. The measured CBD of TPE300 is ~15% lower than the value from the datasheet [47], while for TPU1301, it falls within ~1% difference with the datasheet [46]. The compressibility index shows that TPU1301 with a lower value offers better powder bed packing, while a higher permeability shows its capacity to release the air entrapped within the powder mass. Regarding the aeration ratio, both powders come in well over the threshold of 20 established by Freeman Tech for non-cohesive powders. Moreover, TPE300 presents a mean aeration ratio higher than TPU1301, thus indicating a greater tendency of TPE300 to agglomerate. Finally, the cohesion coefficient values show that TPE300 requires more force to initiate the powder flow. This aspect is important to consider when the powder is transported from the hopper to the building area during the LPBF process.

Table 3. Summary of the rheological properties of TPE300 and TPU1301 measured with FT4 at room temperature.

Test	Powder Characteristics	Units	TPE300	TPU1301
Flow energy	Basic Flow Energy (BFE)	mJ	215.30 ± 1.96	199.96 ± 5.88
	Specific Energy (SE)	mJ/g	6.47 ± 0.07	4.87 ± 0.01
	Conditioned Bulk Density (CBD)	g/cm^3	0.499 ± 0.001	0.507 ± 0.006
Compressibility	Compressibility index	%	12.76 ± 0.28	11.97 ± 0.36
Permeability	Pressure drop	mBar	1.34 ± 0.02	2.01 ± 0.14
Aeration	Aeration Energy	mJ	6.63 ± 1.08	4.83 ± 0.31
	Aeration Ratio	---	32.53 ± 3.35	45.07 ± 2.66
Shear	Cohesion coefficient	kPa	0.137 ± 0.025	0.025 ± 0.011

Overall, considering the above measurements, TPU1301 would seem to be more suitable for the LPBF process than TPE300, with lower interparticular cohesion forces, a lower flow initiation resistance and better bed packing. This conclusion must be accepted with caution, since the flow properties were measured at room temperature and may be affected by the elevated processing temperatures of LPBF [17].

3.2. Bulk Printed Material Characterization

3.2.1. Hardness Testing

Overall, TPE300 samples were significantly harder than their TPU1301 counterparts. Specifically, the measured hardness for TPE300 was 91.6 ± 0.4 Shore A, which represents a −0.5% difference with the 92A value provided by the manufacturer. The measured hardness for TPU1301 was 78.4 ± 0.9 Shore A, representing a −8.8% difference with the 86A hardness indicated by the manufacturer.

3.2.2. Tensile Testing

Typical tensile diagrams of the TPE300 and TPU1301 samples are presented in Figure 8 (tabulated data can be found in Table A3 in the Appendix A). Beyond yielding, the TPE300 samples show strain hardening without necking before the break, which can be associated with the alignment of polymer chains within the structure, something typically seen in rubbery amorphous polymers [5]. For both polymers, the mechanical properties present significant anisotropy, especially in terms of the maximum stress and elongation to failure. As ordinarily seen in LPBF, the mechanical properties in the Z direction are lower than those in the XY direction [11,78]. The stress–strain diagrams corresponding to the 45° direction are close to the former case, but with slightly higher maximum stress and strain values. Overall, the TPE300 samples are significantly more resistant and support much larger strains to failure than their TPU1301 counterparts.

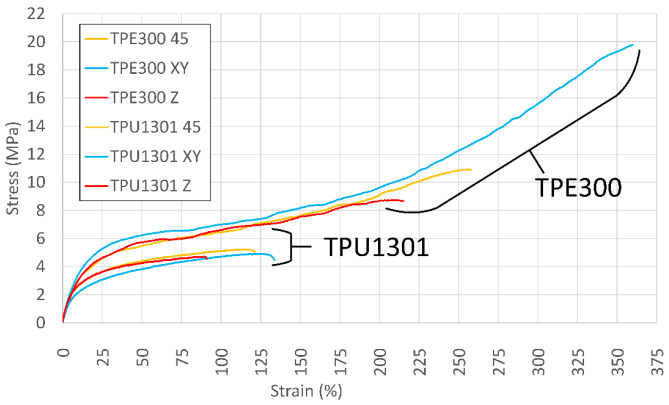

Figure 8. Typical tensile stress–strain diagrams of the TPE300 and TPU1301 samples.

3.3. Phase 1: Varying Unit Cell Design (4 Lattice Structures)

3.3.1. Quasi-Static Compression Testing

Quasi-static testing (Figure 9) showed that the RE samples buckled under loading rather than demonstrating auxetic behavior. This result can be attributed to the inadequacy of the unit cell configuration adopted from the nTop software catalog in terms of providing auxetic behavior [79,80]. Because of the above, the RE unit cell structures were removed from consideration.

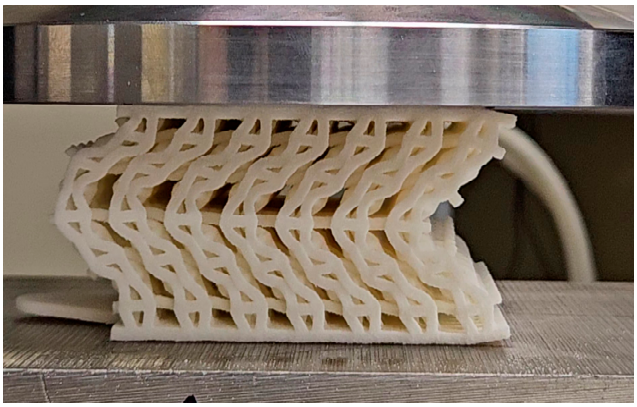

Figure 9. Deformation of RE unit cell during quasi-static compression test.

For the remaining three lattice structures of the study (BC, FC and KE), all the TPE300 structures provide higher energy absorption performance than those from TPU1301, irrespective of the energy absorption indicators used (Figures 4C and 10, Table A4 (Appendix A). The hysteresis loss indicator (Figure 10A) manifests the smallest spread between the maximum and minimum measured values: <5% for the TPE300 structures and <10%, for the TPU1301 structures. Next, the SEA (Figure 10B) and EAeff (Figure 10C) indicators more clearly indicate the higher energy absorption capacities of the TPE300 structures as compared to their TPU1301 counterparts. However, all these indicators embed strains exceeding the densification onset, thus allowing the bulk material to interfere with measurements (see Figure 4C), which is considered unsuitable for rating the energy absorption capacities of the lattice structures. On the other hand, SEAden (Figure 10D), capped by a value of the onset densification strain, offers a clearer distinction between the structures, thus making it better suited for the unit cells' rating. For both materials, therefore, the structures offering the highest level of energy absorption, in the tested configuration, are KE followed by FC and BC. The KE structures manifest ~90% higher SEAden values than do the second-place structures, FC.

Furthermore, compliance, being the inverse of stiffness of the unit cell before yielding, represents the comfort evaluation indicator. The compliance of the TPU1301 structures (Figure 10E) is significantly higher than that of their TPE300 counterparts, which is consistent with the respective bulk hardness values for both materials. The BC structures manifest the highest compliance, with a value 145 and 110% higher than the second- and third-place structures, i.e., FC (TPE300) and KE (TPU1301).

Combining the above quasi-static testing results, it becomes possible to unite both service performance indicators: SEA_{den}, related to energy absorption, and compliance, indicative of wearer comfort (Figure 11). For use in PPE, an ideal unit cell that simultaneously offers the highest level of protection and comfort would tend to be located in the upper right corner of the map, but neither of the unit cells studied in this work can be found in this area. This notwithstanding, the relative positions of the unit cells of this study are identical for both materials, with a broader spread in SEA_{den} for the TPE300 structures (Figure 11A) and a broader spread in compliance for the TPU1301 structures (Figure 11B). Furthermore,

the BC structures offer the highest compliance but the lowest SEA_{den}. In contrast, the KE structures offer the highest SEA_{den} but at the expense of a somewhat lower compliance. Finally, the FC structures present average values for both performance indicators, namely energy absorption and wearer comfort.

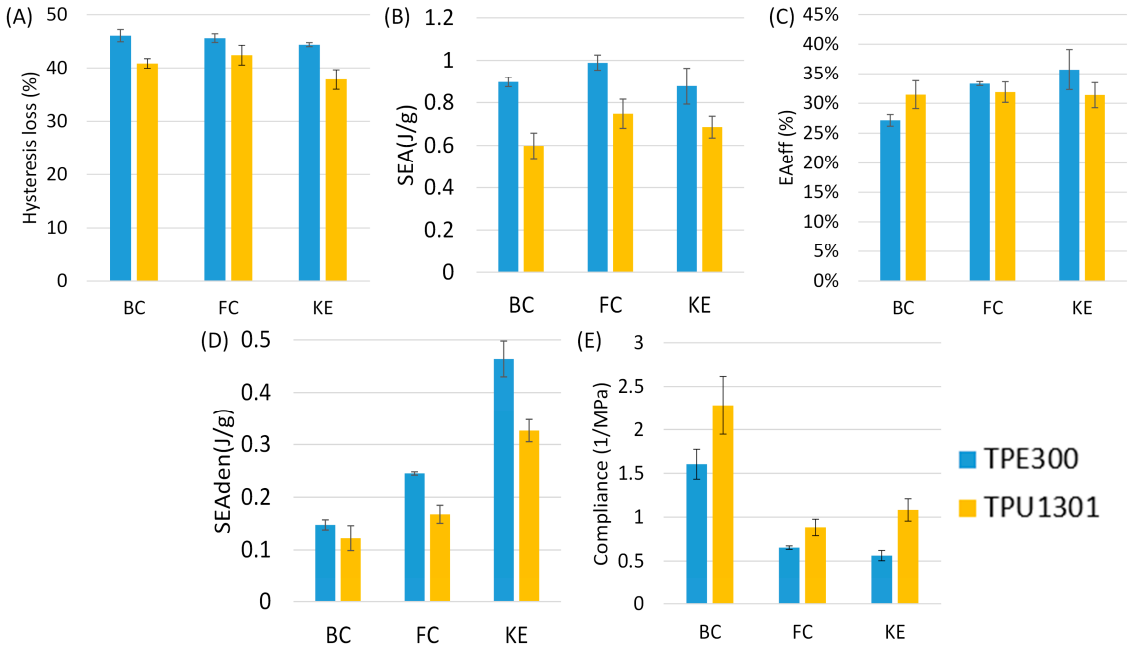

Figure 10. Comparison of the quasi-static performance indicators: (**A**) hysteresis loss, (**B**) SEA, (**C**) EA_{eff}, (**D**) SEA_{den} and (**E**) compliance of the TPE300 and TPU1301 BC, FC and KE unit cells.

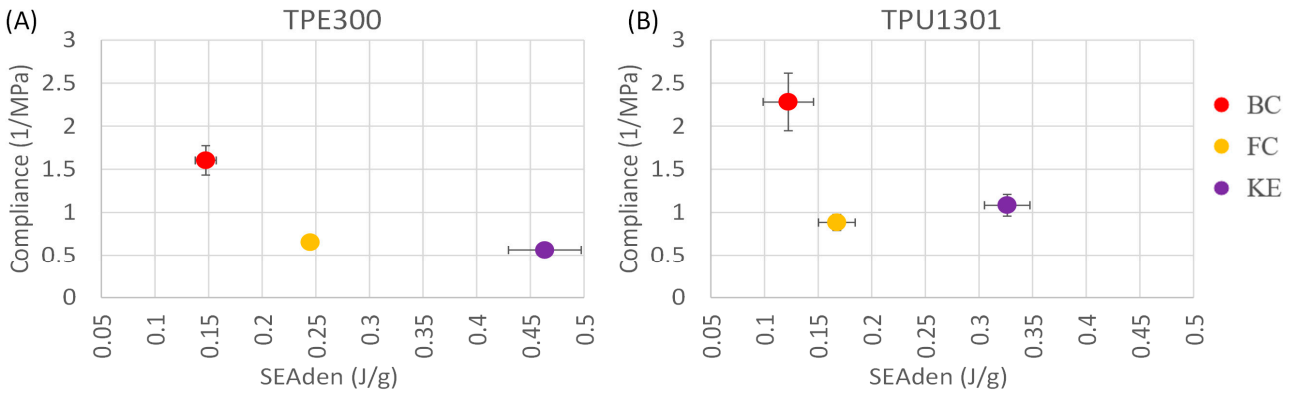

Figure 11. Phase 1 quasi-static testing performance map for the BC, FC and KE lattice structures: (**A**) TPE300 and in (**B**) TPU1301.

3.3.2. Dynamic Compression Testing

Dynamic testing shows that PLAs of the TPE300 unit cells (Figure 12A) are significantly lower than those of the TPU1301 unit cells (Figure 12B), meaning that the former structures offer much better impact protection than the latter. At a sample thickness of 20 mm, the TPU1301 structures have twice the PLA of their TPE300 equivalents. However, the TPE300 structures present an almost three-fold lower sensitivity to thickness variations than their TP1301 counterparts: when the structure thickness increases from 20 to 40 mm, the PLA decreases by 85g for the former as compared to 250g for the latter, and the thicker the sample, the closer the PLA values are for both materials.

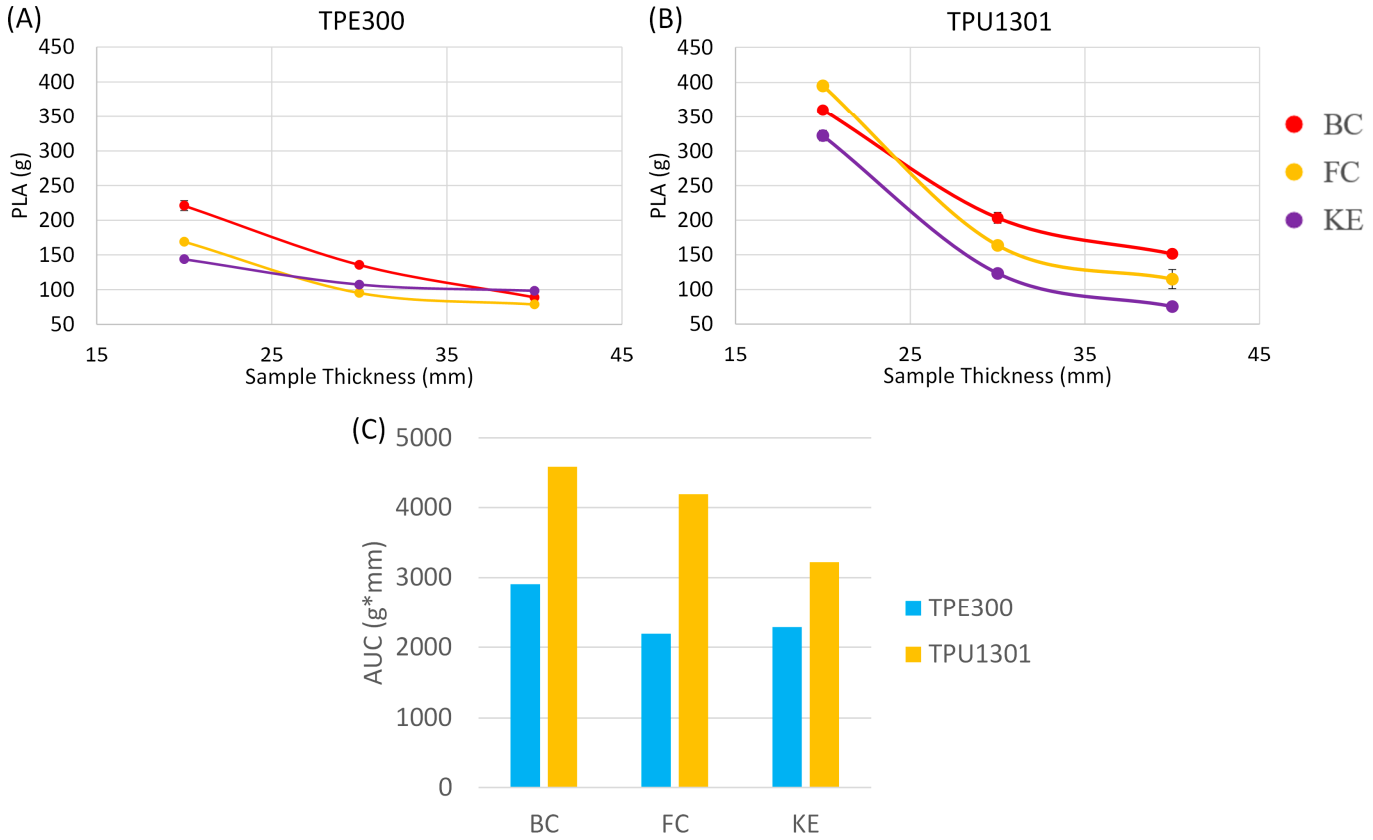

Figure 12. Phase 1: PLA at different sample thicknesses for the unit cells BC, FC and KE: (**A**) TPE300 in (**B**) TPU1301; (**C**) AUC for TPE300 and TPU1301.

3.3.3. Summary of Phase 1 (Unit Cell)

In summary, quasi-static compression testing revealed that the RE unit cells buckled under loading instead of exhibiting auxetic behavior, leading to their removal from consideration. Among the remaining lattice structures (BC, FC and KE), the TPE300 structures demonstrated superior energy absorption as compared to the TPU1301 structures, regardless of the energy absorption indicators used. The KE structures exhibited the highest SEA_{den} values, approximately 90% greater than the FC structures, followed by the BC structures. On the other hand, the TPU1301 structures showed higher compliance that their TPE300 counterparts, with the BC structures leading in this competition. Dynamic compression testing highlighted that the TPE300 unit cells provided significantly lower peak linear acceleration (PLA) values than did the TPU1301 unit cells, demonstrating superior impact protection. Given the need to prioritize energy absorption over comfort, only the KE and FC TPE300 and TPU1301 structures were retained for Phase 2.

3.4. Phase 2: Varying Relative Density (2 Lattice Structures)

With the FC and KE unit cells being selected, the configuration table for Phase 2 (Table 4) can now be filled out. For sample identification, the names of the KE and FC structures are complemented with the letter "D", for density. For example, FC D15 corresponds to the Face-Centered (FC) lattice structure having a density of 15 g/cm^3. Note that all the samples of Phase 2 are built with 10 × 10 × 10 (mm) cells.

Table 4. Configuration and identification of the unit cells studied during the second phase (cell size 10 × 10 × 10 (mm)).

Property	Unit						
Structure		FC	KE	FC	KE	FC	KE
Rel. Density	g/cm^3	0.15		0.2		0.25	
Cell size	mm	10 × 10 × 10					
Feature size	mm	1.52	1.5	1.79	1.76	2.03	1.99
Identification		FC D15	KE D15	FC D20	KE D20	FC D25	KE D25

3.4.1. Quasi-Static Compression Testing

Comparing the TPE300 (Figure 13A) and TPU1301 (Figure 13B) structures, it can be seen that the SEA_{den} and the compliance indicators follow the same trends: the higher the unit cell density, the greater the SEA_{den} and the lower the compliance. For the TPE300 KE structures, SAE_{den} increases from 0.27 (15 g/cm^3) to 0.47 J/g (25 g/cm^3) at the expense of a decrease in compliance from 1.53 to 0.56 MPa^{-1}, thus making them much more protective but stiffer structures than their TPU1301 counterparts. However, for the highest-density (0.25 g/cm^3) KE TPE300 structures, their SEA_{den} values are only 2% higher than those for their intermediate-density (0.20 g/cm^3) equivalents. This shows that beyond a relative density of 0.2 g/cm^3, the TPE300 KE structures do not offer significant improvements in protection. The tabulated data can be found in Table A5 (Appendix A).

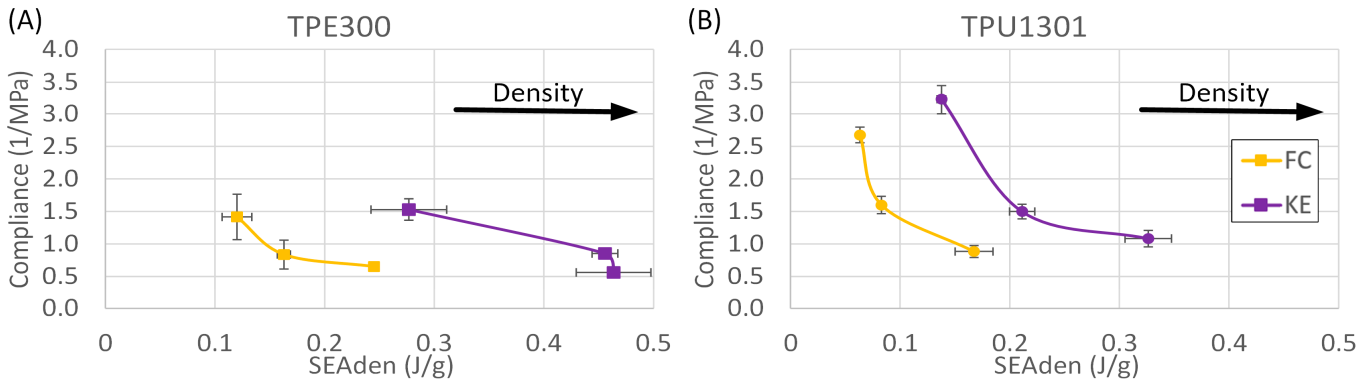

Figure 13. Phase 2 quasi-static testing performance map for the FC and KE lattice structures: (**A**) TPE300 and (**B**) TPU1301.

3.4.2. Dynamic Compression Testing

Identically to the quasi-static testing, increasing the relative density of the TPU1301 and TPE300 structures results in lower PLA values and consequently higher energy absorption (Figure 14). Moreover, the TPE300 structures (Figure 14A) outperform the TPU1301 structures (Figure 14B) for any studied density. Note that to protect the testing equipment, the FC and KE TPU1301 (0.15 g/cm^3) unit cells were not tested in the 20 mm thickness configuration since even more dense (0.20 g/cm^3) 20 mm thick specimens had already shown PLA values close to the maximum permitted 450 g. These absent results are indicated with an "X" on Figure 14B.

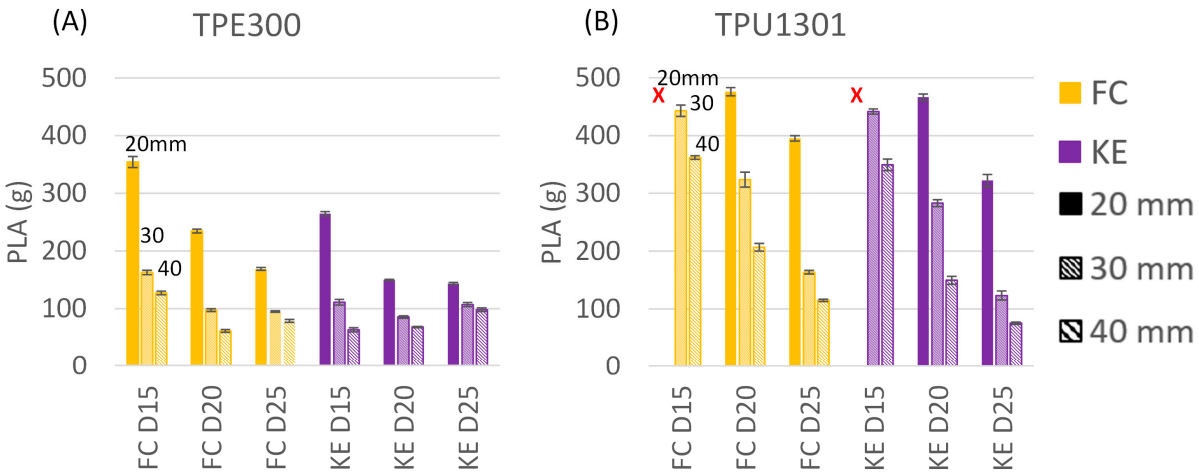

Figure 14. Comparison of PLA for FC and KE unit cells at different densities made with (**A**) TPE300 and (**B**) TPU1301; sign x indicates absent results for 20 mm thick TPU1301 specimens.

3.4.3. Summary of Phase 2 (Density Variation)

In Phase 2, this study focused on varying the relative density of the selected FC and KE structures, all built with 10 × 10 × 10 mm cells. Quasi-static compression testing showed that higher densities led to greater energy absorption and lower compliance for both materials. Similar trends for periodic lattices have been reported by Egan, Khatri [81]; He, Yang [66] and Tancogne-Dejean, Spierings [82].

Overall, the TPU1301 structures displayed higher compliance but lower protection compared to their TPE300 equivalents. Dynamic compression testing further confirmed the TPE300's superior protection performance, with consistently lower PLA values across all densities. For both materials, the KE structures outperformed their FC equivalents in protection capacity. The TPE300 KE structures achieved the highest SEAden values, increasing from 0.27 J/g at 0.15 g/cm^3 to 0.47 J/g at 0.25 g/cm^3, thus making the TPE300 KE combination the most efficient in terms of impact protection, at the expense of a lower level of compliance, varying from 1.50 1/MPa (0.15 g/cm^3) to 0.5 1/MPa (0.25 g/cm^3).

3.5. Phase 3: Varying Cell Size (2 Lattice Structures)

Table 5 presents configurations of the FC and KE structures for the third phase of this study which consisted in variations of a cell size. Note that the relative density of all the structures of this phase is 0.25 g/cm^3. For sample identification, the cell size is preceded by letter "C", for cell. For example, FC C10 corresponds to the Face-Centered (FC) lattice structure built with 10 × 10 × 10 (mm) cells.

Table 5. Configuration and identification of unit cells studied during the third phase (density 0.25 g/cm^3).

Property	Unit						
Structure		FC	KE	FC	KE	FC	KE
Rel. Density	g/cm^3	0.25					
Cell size	mm	10 × 10 × 10		12 × 12 × 12		14 × 14 × 14	
Feature size	mm	2.03	1.99	2.43	2.38	2.84	2.78
Identification		FC C10	KE C10	FC C12	KE C12	FC C14	KE C14

3.5.1. Quasi-Static Compression Testing

Increasing the cell size from 10 × 10 × 10 to 14 × 14 × 14 (mm) has the following impact on the SEA_{den} and compliance values: the larger the cell size, the greater the energy

absorption and compliance, with the KE structures outperforming their FC counterparts. Specifically, for FC, an increase in cell size from 10 × 10 × 10 to 14 × 14 × 14 (mm) leads to an increase in the SEA_{den} from 0.24 to 0.35 J/g (TPE300) and from 0.14 to 0.23 J/g (TPU1301). The same trend is observed for the KE structures: SEA_{den} increases from 0.34 to 0.46 J/g (TPE300) and from 0.25 to 0.33 J/g (TPU1301). As far as compliance is concerned, the larger the cell size of the TPE300 structures, the higher their compliance: it increases by 8% for FC and by 30% for KE. Contrary to TPE300, with an increase in cell size, the compliance of the TPU1301 structures varies within the ±1–3% range, without following a clear trend. Note that, for brevity, these trends are not presented in graphical form.

3.5.2. Dynamic Compression Testing

The dynamic response of the FC and KE lattice structures made of TPE300 and TPU1301 as functions of the cell size are shown in Figure 15. It is important to note that the Y-axis scale for the two graphs is adjusted to offer better visibility.

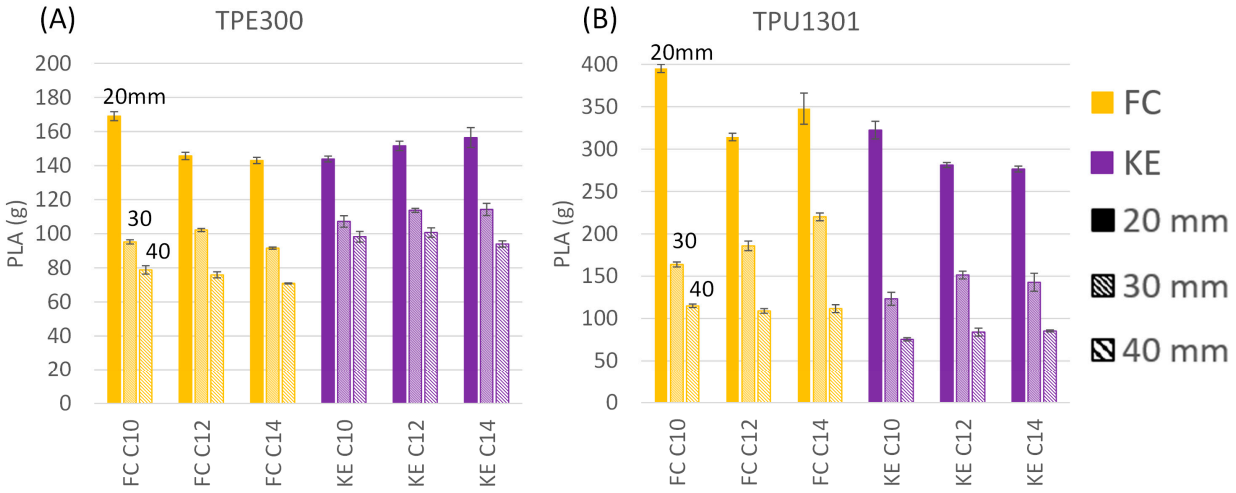

Figure 15. Comparison of the PLA for the FC and KE unit cells with different cell sizes made with (**A**) TPE300 and (**B**) TPU1301.

In line with the trend observed during the first and second phases of this study, the PLA values of the TPE300 structures are significantly lower than those of the TPU1301 ones. Moreover, the thicker the samples, the lower the PLA values, with this reduction being greater for the TPU1301 structures than for the TPE300 structures, for any cell size. Overall, for the 20 mm thick samples, the KE structures made of either TPE300 or TPU1301 slightly outperform the FC structures made of the same materials. For the 30 mm thick samples, however, while the KE structures made of TPU1301 still outperform the FC TPU1301 structures, the situation with the TPE300 structures is the inverse: the FC TPE300 structures perform slightly better than the KE TPE300 structures. The same trend is observed for the 40 mm thick samples: the KE TPU1301 structures perform better than the FC TPU1301 structures, while it is other way around when both structures are printed with TPE300, in which case, the FC structures outperform the KE structures.

3.5.3. Summary of Phase 3 (Cell Size)

Phase 3 focused on varying the cell size for the FC and KE lattice structures at a constant relative density of 0.25 g/cm^3. Quasi-static testing revealed that larger cell sizes improved energy absorption (SEA_{den}) and compliance, with the KE structures outperforming their FC equivalents for both materials. However, their superiority was not as pronounced as stated in the literature [30,66,83]. Dynamic testing confirmed the material-dependent behavior observed earlier where the TPE300 structures exhibited significantly lower peak

linear acceleration (PLA) values than their TPU1301 equivalents, demonstrating better impact protection. Larger cell sizes led to lower PLA values for both materials, with the TPU1301 structures showing a greater improvement. For TPU1301, the KE structures slightly outperformed the FC structures for all the tested thicknesses. For TPE300, the FC structures performed better than their KE counterparts in thicker samples but worser in thinner samples.

4. Discussion and Application Example

In summary, a comparative assessment of the powders' suitability for the LPBF process showed the following: TPU1301 powders manifest a lower resistance to flow and better bed packing than do TPE300 powders, thus facilitating powder spreading during the LPBF process. Moreover, the melting temperature range and the process temperature window of TPU1301 powders are much narrower than those of TPE300 powders, thus requiring better thermal control of the powder bed as part consolidation can prove troublesome for finer details. However, mechanical testing of bulk specimens showed that the printed TPU1301 samples are significantly softer and that their tensile strength and elongation to failure are much lower than those of their TPE300 counterparts.

Moreover, the TPE300 structures display superior energy absorption and lower compliance (higher stiffness) than the TPU1301 structures, irrespective of the unit cell design, KE or FC. Between the lattice geometries, the KE structures globally demonstrate better energy absorption capabilities as compared to the FC structures, regardless of the material used. The only exception is the TPE300 structures with the largest cell size, where the FC structures outperform the KE structures by ~15%. This notwithstanding, the analysis suggests that for applications requiring high energy absorption and structural integrity, TPE300 KE lattices represent the optimal choice.

4.1. Protection–Comfort Map

The correlation analysis shown in Figure 16 highlights the expected relationship in which higher quasi-static energy absorption (SEAden) leads to higher impact absorption (lower AUC). However, the relatively low observed R^2 values (0.68 for TPE300 and 0.40 for TPU1301) highlight the limited predictive capacity of quasi-static testing for the case of dynamic applications. This limitation is due to the differences in testing methodologies as well as the material- and geometry-specific behavior of elastomeric lattices under varying strain rates [1,73]. While it would be ideal to rely on a single test to evaluate both protection and comfort, the exploration presented here proves otherwise, as far as the energy absorption is concerned. Similar conclusions have been reported in [23,66,84,85], where dynamic testing was found to be indispensable. Consequently, for PPE design, dynamic testing remains essential to accurately assess the protection levels and capture complex interactions between the strain rate and material-specific response. Furthermore, while AUC was useful for general rating of the unit cells, this indicator presents the limitation of not reflecting the sensitivity of energy absorption performance to the sample thickness variations. With PPE containing multiple layers of complex shapes and varying thicknesses, it would be ill-advised to use only the agglomerated AUC value as a definitive selection criterion.

Considering this outcome, it was suggested to modify the energy absorption–compliance maps of Figures 11 and 13 by replacing the quasi-statically obtained SEA_{den} values with the dynamically obtained PLA values (both indicators reflecting the energy absorption capacity of structures tested). Note that such a combination, presented in Figure 17, makes perfect sense, since comfort (compliance) is important when no impact is applied (static testing) and it becomes a non-issue in the case of an incident, when the impact protection capacity becomes paramount (dynamic testing). The colored horizontal

lines correspond to the three sample densities we tested (Phase 2), while the oblique lines correspond to the three sample thicknesses we tested (Phase 3). Note that both scales in the TPE300 and TPU1301 maps are adjusted for better readability.

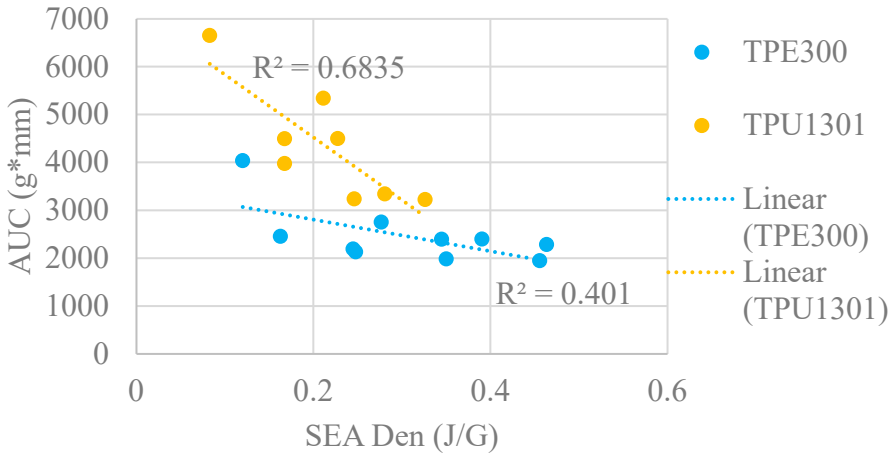

Figure 16. Linear regression of the quasi-static (SEA_{den}) and dynamic (AUC) protection metrics for the FC and KE unit cells in TPE300 and TPU1301.

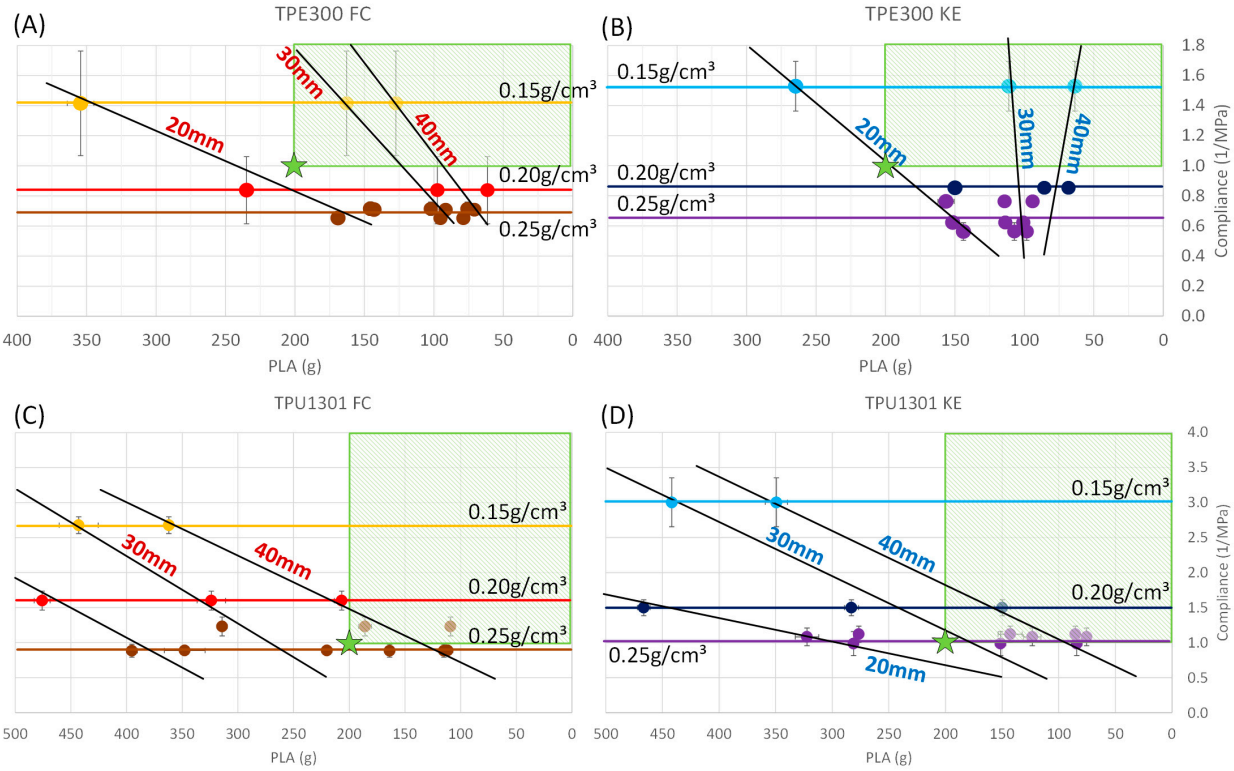

Figure 17. PLA–compliance maps for (**A**) TPE300 FC; (**B**) TPE300 KE; (**C**) TPU1301 FC and (**D**) TPU1301 KE. Safe zones for the application example are highlighted in hatched green, and stars correspond to the minimum requirements of this application example in terms of the impact absorption (PLA) and comfort (compliance).

These charts allow to compare the KE and FC lattice structures made of TPU1301 and TPU300 in terms of their observance of the relevant PPE energy absorption and comfort design criteria. The upper right corner of the graphs corresponds to the location of an ideal high energy absorption and high comfort unit cell. In the design process for a given application, these maps allow to select a structure that will offer an optimal trade-off in terms of the energy absorption and wearer comfort performance criteria.

4.2. Application Example

As an example, let us use the design–performance maps of Figure 17 to select an appropriate structure for a PPE liner. Let us consider a protective liner with a maximum PLA of 200 g and a minimum compliance of 1.0 MPa^{-1} (both values are arbitrary). From these guidelines, it is possible to delimit an area where the PLA is minimized and the comfort (compliance) is maximized (green hatched area of Figure 17). In the case where the thickness is not a constraint, the best structure would be the one that provides the required minimum levels of protection ($\leq$200 g) and comfort ($\geq$1 MPa^{-1}) while having the smallest thickness and the lowest density, i.e., the most compact and lightest. Considering these design objectives, the minimum thickness and density of the TPE300 and TPU1301 KE and FC structures can be found by interpolation in Figure 17 and collected in Table 6. From this example, it appears that to meet the design requirements ($\leq$200 g and $\geq$1 MPa^{-1}) using the KE lattices (10 $\times$ 10 $\times$ 10 mm unit cell), we need either a 20 mm thick, 0.18 g/cm^3 dense TPE300 structure or a 25 mm thick, 0.25 g/cm^3 dense TPU1301 structure.

Table 6. Numerical values interpolated and calculated for the application example.

		Thickness	**Density**	**Area Density**	**Weight of a 100 mm^2-Area Liner**
Material	Unit Cell	mm	g/cm^3	g/cm^2	g
TPE300	FC	22	0.18	0.40	39.6
	KE	20	0.18	0.36	36.0
TPU1301	FC	35	0.25	0.88	87.5
	KE	25	0.25	0.63	62.5

Now, if we were to decide to protect an arbitrary 100 mm^2 surface area using the KE liner with the aforementioned requirements, the density–thickness values taken from Figure 17 and Table 6 for TPE300 and TPU1301 would result in a two-fold difference in weight of the corresponding liners: 36 g for the former as compared to 62.5 g for the latter. Moreover, if TPU1301 is now considered as a protective material, the use of the FC liner instead of its KE counterpart would result in a 40% heavier product: 87.5 g for the former versus 62.5 g for the latter.

5. Study Limitations and Future Scope

While this study provides valuable insights into the mechanical behavior and performance of lattice structures for PPE applications, there are certain limitations that should be acknowledged to place the findings in context. These limitations highlight areas where further research is required to enhance the robustness of our conclusions and address factors that may influence the reliability and applicability of the obtained results.

The current study did not directly investigate the effects of powder reuse and aging on the mechanical properties of printed parts, which is a critical aspect to consider for additive manufacturing processes. Repeated use of powder, particularly TPU1301, on a smaller EOS P110 printer may introduce variabilities caused by an increased exposure to environmental factors such as humidity and temperature fluctuations. These factors could potentially alter the powder characteristics such as flowability, packing density and thermal behavior, impacting both the printing process and the quality and mechanical properties of printed parts. The increased number of print jobs required for TPU1301 as compared to TPE300, which were processed using a larger EOS P770 printer, further amplifies the likelihood of powder deterioration. While the literature on powder aging is more comprehensive for polyamides [86–89], there is a dearth of studies focusing on elastomeric materials [16,90], which limits the capacity to draw robust conclusions. However, as previously stated, in the present study, the powder refreshment procedures recommended by EOS were

followed to mitigate the powder aging phenomenon. Future research should explore long-term powder aging effects in elastomeric powders under diverse processing conditions to provide a clearer understanding of their implications on the geometry and properties of printed structures.

While it was acknowledged in the methodology section, the fabrication anisotropy of the structure was not studied. For instance, the layer-wise nature of LPBF fabrication would inherently result in directional strength and stiffness dependencies, particularly in the Z direction. Moreover, anisotropy coupled with powder aging could have a detrimental effect on the structural performance.

A correlation analysis between quasi-static energy absorption (SEAden) and dynamic energy absorption (AUC) indicators revealed an expected relationship, but with relatively low correlation coefficient values (R^2 values = 0.68 for TPE300 and 0.40 for TPU1301). These values highlight the challenges that lie in translating quasi-static test results into dynamic performance predictions, which stem from fundamental differences in the testing methodologies and loading rates. The mechanical behavior of elastomeric powders under varying strain rates, coupled with material-specific viscoelastic properties, likely contribute to this discrepancy. Additionally, external factors such as manufacturing inconsistencies, sample geometry variations and environmental influences during testing could further affect the observed correlations. Notwithstanding these limitations, the complementary nature of the quasi-static and dynamic indicators provides valuable insights into the mechanical behavior of lattice structures. Addressing the stated challenges through refined testing protocols, multi-scale modeling approaches and additional performance metrics could enhance the reliability and practical applicability of such analyses in future studies.

The present study did not investigate the impact of vapor smoothing on the mechanical and functional properties of lattice structures. Vapor smoothing, commonly used to enhance surface finish and reduce roughness [91], may significantly alter the dimensions and geometry of delicate structures, potentially affecting key performance indicators such as compliance and energy absorption. Additionally, the chemical exposure involved in this process could introduce residual stresses or affect interlayer bonding, particularly in elastomeric materials, which may compromise durability under dynamic loading. While vapor smoothing is widely recognized as a beneficial post-processing technique, its long-term effects on material stability and mechanical behavior under varying environmental conditions remain unclear. Future studies should explore these aspects to better understand the trade-offs associated with vapor smoothing and optimize its parameters for PPE applications.

Finally, the present study does not include a direct comparison between the 3D-printed lattice structures and conventional foams commonly used in PPE. Such a comparison would provide valuable insights into the relative mechanical performance, particularly in terms of energy absorption and compliance. Conventional foams have long served as the standard in PPE due to their predictable behavior and ease of processing. However, additively manufactured lattices offer significantly greater design flexibility and the capacity for localized property tuning, potentially leading to superior performance under impact conditions. In future work, it will be important to systematically evaluate the performance of conventional foams under the same testing protocols as those used in this study. This will not only contextualize our findings but also highlight the trade-offs and potential advantages of using 3D-printed lattices over traditional materials. By doing so, it will be possible to provide a more comprehensive framework for material selection and design optimization in PPE applications.

6. Conclusions

This study compared the mechanical performance of three lattice structures, namely Kelvin, Face-Centered Cubic and Body-Centered Cubic, for potential use in personal

protective equipment (PPE). They were manufactured from two elastomeric powders, TPU1301 and TPE300, using two laser powder bed fusion (LPBF) EOS printers: P110 for the former and P770 for the latter. Key findings indicate that Kelvin and Face-Centered Cubic lattices manifest the best balance (trade-off) between energy absorption and user comfort across all the tested densities, cell sizes and sample thicknesses. After manufacturing, all the structures were tested in compression using both the quasi-static mode and dynamic mode in conformity with the state of the art and standards established for PPE.

Based on the dynamic and quasi-static testing results, an original protection–comfort map was proposed. Such a map offers the possibility to design Kelvin unit cell-based protective liners manufactured from TPE300 powders, thus offering a lightweight and compact solution with superior performance in terms of both energy absorption and wearer comfort. These results highlight the promise of architectured lattices fabricated by laser powder bed fusion in advancing the design of innovative PPE. Future research should explore multi-scale lattice configurations and post-processing techniques such as vapor polishing, as well as broaden material options to further enhance the functionality and commercialization of high-performance PPE.

Author Contributions: Conceptualization, T.K.; Data curation, W.T.T.; Formal analysis, W.T.T. and A.C.; Funding acquisition, V.B.; Investigation, A.C. and W.T.T.; Methodology, W.T.T., A.C. and V.B.; Project administration, V.B.; Resources, T.K.; Software, W.T.T. and A.C.; Supervision, T.K. and V.B.; Validation, W.T.T. and A.C.; Visualization, A.C. and V.B.; Writing—original draft, W.T.T. and V.B.; Writing—review and editing, W.T.T. and V.B. All authors have read and agreed to the published version of the manuscript.

Funding: This work was financially supported by the Mitacs Accelerate program [grant number IT 35346].

Data Availability Statement: Upon request.

Acknowledgments: The authors are grateful to S. Plamondon (mechanical testing) and R. Romanica (general support), technicians in the laboratories of ÉTS, for their technical support.

Conflicts of Interest: Author Thierry Krick was employed by the company Bauer Hockey LTD. The remaining authors declare that the research was conducted in the absence of any commercial or financial relationships that could be construed as a potential conflict of interest.

Appendix A

Table A1. Particle size distribution measured for both powders.

		TPE300	TPU1301
Mean	µm	81.33 ± 0.58	85.78 ± 0.24
Median	µm	81.96 ± 0.65	84.20 ± 0.42
D_{10}	µm	26.97 ± 0.64	22.17 ± 0.14
D_{50}	µm	81.96 ± 0.65	84.20 ± 0.42
D_{90}	µm	135.00 ± 0.83	150.50 ± 0.20
Standard deviation	µm	40.06 ± 0.21	48.42 ± 0.11

Table A2. Thermal properties of TPE300 and TPU1301 powders.

Property	Symbol	Unit	TPE300	TPU1301
Glass Transition	T_g	°C	50.5	42.6
Melting Onset	$T_{m,on}$	°C	115.3	119.8
Melting Peak	$T_{m,peak}$	°C	134.5	130.5
Melting End	$T_{m,end}$	°C	167.6	150.3
Melting Peak Width	$T_{m,width}$	°C	52.3	30.5

Table A2. *Cont.*

Property	Symbol	Unit	TPE300	TPU1301
Endo Heat Flow Peak	$Q_{Endo,peak}$	W/g	0.30	0.29
Endo Heat Flow Peak Height	$Q_{Endo,peak\_height}$	W/g	0.058	0.115
Normalized Endo Enthalpy	$H_{n,\ endo}$	J/g	13.7	16.73
Crystallization Onset	$T_{c,on}$	°C	82.4	117.82
Crystallization Peak	$T_{c,peak}$	°C	72.3	109.08
Crystallization End	$T_{c,end}$	°C	61.7	100.22
Crystallization Peak Width	$T_{c,\ width}$	°C	20.7	17.6
Normalized Exo Enthalpy	$H_{n,\ exo}$	J/g	11.9	10.38
Exo Heat Flow Peak	$Q_{Exo,peak}$	W/g	−0.40	−0.36
Exo Heat Flow Peak Height	$Q_{Exo,peak\_height}$	W/g	−0.158	−0.141

Table A3. Summary of the measured tensile properties of TPE300 and TPU1301.

Orientation		XY		Z		45	
Material		TPE300	TPU1301	TPE300	TPU1301	TPE300	TPU1301
Elastic modulus	MPa	34.97 ± 0.94	47.76 ± 7.80	31.83 ± 1.59	69.25 ± 11.89	29.89 ± 1.12	61.89 ± 7.25
Tangent Modulus	MPa	2.28 ± 0.14	1.67 ± 0.12	2.08 ± 0.10	1.74 ± 0.12	2.24 ± 0.05	1.65 ± 0.08
Yield Strength	MPa	5.26 ± 0.18	3.00 ± 0.18	4.74 ± 0.14	3.52 ± 0.11	4.44 ± 0.09	3.59 ± 0.09
Tensile Strength	MPa	20.49 ± 0.96	4.90 ± 0.37	8.80 ± 0.35	5.00 ± 0.26	11.04 ± 0.31	5.30 ± 0.16
Tensile Strain	%	361.1 ± 4.2	120.5 ± 16.9	205.7 ± 9.2	88.9 ± 9.5	254.8 ± 7.1	113.5 ± 8.1
Strain at break	%	362.5 ± 4.6	134.4 ± 17.1	211.6 ± 9.2	94.4 ± 8.9	258.8 ± 7.0	119.8 ± 9.3

Table A4. Summary of the measured quasi-static properties of the unit cells studied in TPE300 and TPU1301.

Property	EAeff (%)		Hysteresis Loss (%)		SEAden (J/G)		Compliance (1/MPa)	
Material	TPE300	TPU1301	TPE300	TPU1301	TPE300	TPU1301	TPE300	TPU1301
BC	0.27 ± 0.01	0.31 ± 0.03	46.08 ± 1.15	40.85 ± 0.90	0.15 ± 0.01	0.12 ± 0.02	1.60 ± 0.17	2.28 ± 0.33
FC	0.33 ± 0.01	0.32 ± 0.02	45.61 ± 0.81	42.42 ± 1.85	0.24 ± 0.00	0.17 ± 0.02	0.65 ± 0.02	0.88 ± 0.09
KE	0.36 ± 0.01	0.31 ± 0.00	44.39 ± 0.39	37.81 ± 1.85	0.46 ± 0.03	0.33 ± 0.02	0.56 ± 0.06	1.08 ± 0.13

Table A5. Summary of the measured quasi-static properties of the FC and KE unit cell density variation made in TPE300 and TPU1301.

Property	EAeff (%)		Hysteresis Loss (%)		SEAden (J/G)		Compliance (1/MPa)	
Material	TPE300	TPU1301	TPE300	TPU1301	TPE300	TPU1301	TPE300	TPU1301
FC D10 C10	0.39 ± 0.01	0.35 ± 0.05	45.68 ± 0.33	51.32 ± 2.74	0.07 ± 0.01	0.03 ± 0.00	2.07 ± 0.14	8.87 ± 1.86
FC D15 C10	0.40 ± 0.08	0.34 ± 0.01	50.64 ± 3.16	43.73 ± 1.53	0.12 ± 0.01	0.06 ± 0.00	1.42 ± 0.35	2.68 ± 0.12
FC D20 C10	0.36 ± 0.03	0.31 ± 0.00	46.29 ± 2.16	44.14 ± 0.24	0.16 ± 0.01	0.08 ± 0.00	0.84 ± 0.22	1.60 ± 0.13
FC D25 C10	0.33 ± 0.01	0.32 ± 0.02	45.61 ± 0.81	42.42 ± 1.85	0.24 ± 0.00	0.17 ± 0.02	0.65 ± 0.02	0.88 ± 0.09
KE D10 C10	0.49 ± 0.03	0.35 ± 0.01	33.92 ± 4.08	36.49 ± 0.02	0.23 ± 0.05	0.07 ± 0.00	3.06 ± 0.00	12.73 ± 1.80
KE D15 C10	0.40 ± 0.01	0.34 ± 0.01	38.27 ± 3.15	36.74 ± 1.17	0.28 ± 0.03	0.14 ± 0.00	1.53 ± 0.17	3.23 ± 0.22
KE D20 C10	0.36 ± 0.01	0.35 ± 0.00	40.41 ± 1.77	37.14 ± 0.70	0.24 ± 0.00	0.21 ± 0.01	0.85 ± 0.04	1.50 ± 0.11
KE D25 C10	0.36 ± 0.01	0.31 ± 0.00	44.39 ± 0.39	37.81 ± 1.85	0.46 ± 0.01	0.33 ± 0.02	0.56 ± 0.06	1.08 ± 0.13

References

1. Ashby, M.F.; Gibson, L.J. *Cellular Solids: Structure and Properties*; Press Syndicate of the University of Cambridge: Cambridge, UK, 1997; pp. 175–231.
2. Shrivastava, A. *Introduction to Plastics Engineering*; William Andrew: Norwich, NY, USA, 2018.
3. Bhowmick, A.K.; Stephens, H. *Handbook of Elastomers*; CRC Press: Boca Raton, FL, USA, 2000.
4. Hepburn, C. *Polyurethane Elastomers*; Springer Science & Business Media: Berlin, Germany, 2012.
5. Callister, W.D., Jr.; Rethwisch, D.G. *Callister's Materials Science and Engineering*; John Wiley & Sons: Hoboken, NJ, USA, 2020.
6. Drobny, J.G. *Handbook of Thermoplastic Elastomers*; Elsevier: Amsterdam, The Netherlands, 2014.

7. Verbelen, L.; Dadbakhsh, S.; Eynde, M.V.D.; Strobbe, D.; Kruth, J.-P.; Goderis, B.; Van Puyvelde, P. Analysis of the material properties involved in laser sintering of thermoplastic polyurethane. *Addit. Manuf.* **2017**, *15*, 12–19. [CrossRef]
8. Eceiza, A.; Martin; de la Caba, K.; Kortaberria, G.; Gabilondo, N.; Corcuera, M.; Mondragon, I. Thermoplastic polyurethane elastomers based on polycarbonate diols with different soft segment molecular weight and chemical structure: Mechanical and thermal properties. *Polym. Eng. Sci.* **2007**, *48*, 297–306. [CrossRef]
9. Zhao, Z.; Li, X.; Jiang, H.; Su, X.; Zhang, X.; Zou, M. Study on the Mechanical Properties and Energy Absorbing Capability of Polyurethane Microcellular Elastomers under Different Compressive Strain Rates. *Polymers* **2023**, *15*, 778. [CrossRef]
10. Smith, T.L. Strength of elastomers—A perspective. *Polym. Eng. Sci.* **2004**, *17*, 129–143. [CrossRef]
11. Goodridge, R.; Ziegelmeier, S. Powder bed fusion of polymers. In *Laser Additive Manufacturing*; Woodhead Publishing: Sawston, UK, 2017; pp. 181–204.
12. Chatham, C.A.; Long, T.E.; Williams, C.B. A review of the process physics and material screening methods for polymer powder bed fusion additive manufacturing. *Prog. Polym. Sci.* **2019**, *93*, 68–95. [CrossRef]
13. Wang, Y.; Xu, Z.; Wu, D.; Bai, J. Current status and prospects of polymer powder 3D printing technologies. *Materials* **2020**, *13*, 2406. [CrossRef]
14. Dadbakhsh, S.; Verbelen, L.; Vandeputte, T.; Strobbe, D.; Van Puyvelde, P.; Kruth, J.-P. Effect of Powder Size and Shape on the SLS Processability and Mechanical Properties of a TPU Elastomer. *Phys. Procedia* **2016**, *83*, 971–980. [CrossRef]
15. Plummer, K.; Vasquez, M.; Majewski, C.; Hopkinson, N. Study into the recyclability of a thermoplastic polyurethane powder for use in laser sintering. *Proc. Inst. Mech. Eng. Part B J. Eng. Manuf.* **2012**, *226*, 1127–1135. [CrossRef]
16. Ziegelmeier, S.; Wöllecke, F.; Tuck, C.J.; Goodridge, R.D.; Hague, R.J. Aging behavior of thermoplastic elastomers in the laser sintering process. *Mater. Res.* **2014**, *29*, 1841–1851. [CrossRef]
17. Eynde, M.V.D.; Verbelen, L.; Van Puyvelde, P. Assessing polymer powder flow for the application of laser sintering. *Powder Technol.* **2015**, *286*, 151–155. [CrossRef]
18. Xu, T.; Shen, W.; Lin, X.; Xie, Y.M. Mechanical Properties of Additively Manufactured Thermoplastic Polyurethane (TPU) Material Affected by Various Processing Parameters. *Polymers* **2020**, *12*, 3010. [CrossRef] [PubMed]
19. Ciobotaru, V.; Batistella, M.; Emmer, E.D.O.; Clari, L.; Masson, A.; Decante, B.; Le Bret, E.; Lopez-Cuesta, J.-M.; Hascoet, S. Aortic Valve Engineering Advancements: Precision Tuning with Laser Sintering Additive Manufacturing of TPU/TPE Submillimeter Membranes. *Polymers* **2024**, *16*, 900. [CrossRef] [PubMed]
20. Gibson, L.J. Biomechanics of cellular solids. *J. Biomech.* **2005**, *38*, 377–399. [CrossRef]
21. Maconachie, T.; Leary, M.; Lozanovski, B.; Zhang, X.; Qian, M.; Faruque, O.; Brandt, M. SLM lattice structures: Properties, performance, applications and challenges. *Mater. Des.* **2019**, *183*, 108137. [CrossRef]
22. Scheffler, M.; Colombo, P. *Cellular Ceramics: Structure, Manufacturing, Properties and Applications*; John Wiley & Sons: Hoboken, NJ, USA, 2006.
23. Yin, H.; Zhang, W.; Zhu, L.; Meng, F.; Liu, J.; Wen, G. Review on lattice structures for energy absorption properties. *Compos. Struct.* **2022**, *304*, 116397. [CrossRef]
24. Greco, A.; Lionetto, F. The influence of the stress relaxation and creep recovery times on the viscoelastic properties of open cell foams. *Polym. Eng. Sci.* **2009**, *49*, 1142–1150. [CrossRef]
25. Ebe, K.; Griffin, M.J. Factors affecting static seat cushion comfort. *Ergonomics* **2001**, *44*, 901–921. [CrossRef]
26. Zhang, X.; Li, Q.; Niu, J.; Chen, X.; Zu, Y. A Novel Method for Evaluating the Suitability of Helmets. *Hum. Factors Wearable Technol.* **2023**, *85*, 121–127.
27. Bloodworth-Race, S.; Critchley, R.; Hazael, R.; Peare, A.; Temple, T. Testing the blast response of foam inserts for helmets. *Heliyon* **2021**, *7*, e06990. [CrossRef]
28. Hilyard, N.A.; Cunningham, A. (Eds.) *Low Density Cellular Plastics: Physical Basis of Behaviour*; Springer Science & Business Media: Berlin, Germany, 2012.
29. Dong, G.; Tang, Y.; Zhao, Y.F. A survey of modeling of lattice structures fabricated by additive manufacturing. *J. Mech. Des.* **2017**, *139*, 100906. [CrossRef]
30. Park, K.-M.; Roh, Y.-S.; Lee, B.-C. Effects of the unit-cell size and arrangement on the compressive behaviors of lattice structures in powder bed fusion additive manufacturing. *Results Mater.* **2024**, *22*, 100587. [CrossRef]
31. Ozdemir, Z.; Hernandez-Nava, E.; Tyas, A.; Warren, J.A.; Fay, S.D.; Goodall, R.; Todd, I.; Askes, H. Energy absorption in lattice structures in dynamics: Experiments. *Int. J. Impact Eng.* **2016**, *89*, 49–61. [CrossRef]
32. Amaechi, C.V.; Adefuye, E.F.; Kgosiemang, I.M.; Huang, B.; Amaechi, E.C. Scientometric Review for Research Patterns on Additive Manufacturing of Lattice Structures. *Materials* **2022**, *15*, 5323. [CrossRef] [PubMed]
33. Cronau, J.; Engstler, F. Energy absorption of 3D printed stochastic lattice structures under impact loading—Design parameters, manufacturing, and testing. *Prog. Addit. Manuf.* **2025**, *10*, 3145–3156. [CrossRef]
34. Decker, T.; Kedziora, S. Optimizing the Thickness of Functionally Graded Lattice Structures for High-Performance Energy Absorption: A Case Study Based on a Bicycle Helmet. *Appl. Sci.* **2024**, *14*, 2788. [CrossRef]

35. Maskery, I.; Sturm, L.; Aremu, A.O.; Panesar, A.; Williams, C.B.; Tuck, C.J.; Wildman, R.D.; Ashcroft, I.; Hague, R.J.M. Insights into the mechanical properties of several triply periodic minimal surface lattice structures made by polymer additive manufacturing. *Polymer* **2018**, *152*, 62–71. [CrossRef]
36. Habib, F.; Iovenitti, P.; Masood, S.; Nikzad, M.; Ruan, D. Design and evaluation of 3D printed polymeric cellular materials for dynamic energy absorption. *Int. J. Adv. Manuf. Technol.* **2019**, *103*, 2347–2361. [CrossRef]
37. Bai, L.; Gong, C.; Chen, X.; Sun, Y.; Xin, L.; Pu, H.; Peng, Y.; Luo, J. Mechanical properties and energy absorption capabilities of functionally graded lattice structures: Experiments and simulations. *Int. J. Mech. Sci.* **2020**, *182*, 105735. [CrossRef]
38. Cerardi, A.; Caneri, M.; Meneghello, R.; Concheri, G.; Ricotta, M. Mechanical characterization of polyamide cellular structures fabricated using selective laser sintering technologies. *Mater. Des.* **2013**, *46*, 910–915. [CrossRef]
39. Dwyer, C.M.; Carrillo, J.G.; De la Peña, J.A.D.; Santiago, C.C.; MacDonald, E.; Rhinehart, J.; Williams, R.M.; Burhop, M.; Yelamanchi, B.; Cortes, P. Impact Performance of 3D Printed Spatially Varying Elastomeric Lattices. *Polymers* **2023**, *15*, 1178. [CrossRef]
40. Diosdado-De la Peña, J.A.; Dwyer, C.M.; Krzeminski, D.; MacDonald, E.; Saldaña-Robles, A.; Cortes, P.; Choo, K. Low Impact Velocity Modeling of 3D Printed Spatially Graded Elastomeric Lattices. *Polymers* **2022**, *14*, 4780. [CrossRef] [PubMed]
41. Yuan, S.; Shen, F.; Bai, J.; Chua, C.K.; Wei, J.; Zhou, K. 3D soft auxetic lattice structures fabricated by selective laser sintering: TPU powder evaluation and process optimization. *Mater. Des.* **2017**, *120*, 317–327. [CrossRef]
42. OSHA. *Personal Protective Equipment*; Labor, D.o., Ed.; OSHA: Washington, DC, USA, 2004.
43. Brown, S.A.T.; DeSimone, L.; Garlie, T.N.; Mitchell, K.B. Get Comfortable Being Uncomfortable: Variability in the Assessment of Perceived Comfort During Clothing and Individual Equipment Evaluations. *Proc. Hum. Factors Ergon. Soc. Annu. Meet.* **2018**, *62*, 2023–2027. [CrossRef]
44. Scarfato, P.; Di Maio, L.; Incarnato, L. Structure and physical-mechanical properties related to comfort of flexible polyurethane foams for mattress and effects of artificial weathering. *Compos. Part B Eng.* **2017**, *109*, 45–52. [CrossRef]
45. Zhou, X.; Nie, J.; Song, B.; Yang, Q.; Xu, X.; Xu, J.; Zhang, Q.; Ding, L. Ergonomic evaluation of thermal comfort for different outlet distribution patterns and ventilation conditions in the pilot protective helmet. *Appl. Therm. Eng.* **2023**, *226*, 120355. [CrossRef]
46. EOS GmbH. *EOS TPU 1301 Material Datasheet*; EOS GmbH: Krailling, Germany, 2020; p. 2.
47. ALM. *TPE300 DataSheet*; Advanced Laser Materials: Temple, TX, USA, 2021.
48. *ASTM E1131-20*; Standard Test Method for Compositional Analysis by Thermogravimetry. ASTM International: West Conshohocken, PA, USA, 2020.
49. *ASTM D3418-21*; Standard Test Method for Transition Temperatures and Enthalpies of Fusion and Crystallization of Polymers by Differential Scanning Calorimetry. ASTM International: West Conshohocken, PA, USA, 2021.
50. EOS GmbH. *EOS TPU 1301 Application Notes*; EOS GmbH: Krailling, Germany, 2020; p. 2.
51. *ASTM D1895-17*; Standard Test Methods for Apparent Density, Bulk Factor, and Pourability of Plastic Materials. ASTM International: West Conshohocken, PA, USA, 2017.
52. Klamert, V.; Schiefermair, L.; Bublin, M.; Otto, A. In Situ Analysis of Curling Defects in Powder Bed Fusion of Polyamide by Simultaneous Application of Laser Profilometry and Thermal Imaging. *Appl. Sci.* **2023**, *13*, 7179. [CrossRef]
53. Mousa, A.A. Experimental investigations of curling phenomenon in selective laser sintering process. *Rapid Prototyp. J.* **2016**, *22*, 405–415. [CrossRef]
54. Ajoku, U.; Saleh, N.; Hopkinson, N.; Hague, R.; Erasenthiran, P. Investigating mechanical anisotropy and end-of-vector effect in laser-sintered nylon parts. *Proc. Inst. Mech. Eng. Part B J. Eng. Manuf.* **2006**, *220*, 1077–1086. [CrossRef]
55. Goodridge, R.D.; Tuck, C.J.; Hague, R.J.M. Laser sintering of polyamides and other polymers. *Prog. Mater. Sci.* **2012**, *57*, 229–267. [CrossRef]
56. Brighenti, R.; Cosma, M.P.; Marsavina, L.; Spagnoli, A.; Terzano, M. Laser-based additively manufactured polymers: A review on processes and mechanical models. *J. Mater. Sci.* **2020**, *56*, 961–998. [CrossRef]
57. *ASTM D2240-15*; Standard Test Method for Rubber Property—Durometer Hardness. ASTM International: West Conshohocken, PA, USA, 2021.
58. *ASTM D638-14*; Standard Test Method for Tensile Properties of Plastics. ASTM International: West Conshohocken, PA, USA, 2015.
59. Mueller, J.; Matlack, K.H.; Shea, K.; Daraio, C. Energy Absorption Properties of Periodic and Stochastic 3D Lattice Materials. *Adv. Theory Simul.* **2019**, *2*, 1900081. [CrossRef]
60. Yu, S.; Sun, J.; Bai, J. Investigation of functionally graded TPMS structures fabricated by additive manufacturing. *Mater. Des.* **2019**, *182*, 108021. [CrossRef]
61. Nelson, J.C. *Selective Laser Sintering: A Definition of The Process and an Empirical Sintering Model*; The University of Texas at Austin: Austin, TX, USA, 1993.
62. Riedlbauer, D.; Drexler, M.; Drummer, D.; Steinmann, P.; Mergheim, J. Modelling, simulation and experimental validation of heat transfer in selective laser melting of the polymeric material PA12. *Comput. Mater. Sci.* **2014**, *93*, 239–248. [CrossRef]
63. Bourell, D.L.; Wohlers, T. *Introduction to Additive Manufacturing*; ASM International: Novelty, OH, USA, 2020; pp. 3–10.

64. Bottlang, M.; DiGiacomo, G.; Tsai, S.; Madey, S. Effect of helmet design on impact performance of industrial safety helmets. *Heliyon* **2022**, *8*, e09962. [CrossRef]
65. Foster, L.; Peketi, P.; Allen, T.; Senior, T.; Duncan, O.; Alderson, A. Application of auxetic foam in sports helmets. *Appl. Sci.* **2018**, *8*, 354. [CrossRef]
66. He, G.; Yang, H.; Chen, T.; Ning, Y.; Zou, H.; Zhu, F. Lattice Structure Design Method Aimed at Energy Absorption Performance Based on Bionic Design. *Machines* **2022**, *10*, 965. [CrossRef]
67. Yoder, M.; Thompson, L.; Summers, J. Size effects in lattice-structured cellular materials: Edge softening effects. *J. Mater. Sci.* **2018**, *54*, 3942–3959. [CrossRef]
68. Ramirez, B.J.; Misra, U.; Gupta, V. Viscoelastic foam-filled lattice for high energy absorption. *Mech. Mater.* **2018**, *127*, 39–47. [CrossRef]
69. *ISO/ASTM DIS52959*; Additive Manufacturing of metals—Test artefacts—Compression validation coupons for lattice designs. ASTM International: Novelty, OH, USA, 2024; p. 14.
70. *ASTM D3574-17*; Standard Test Methods for Flexible Cellular Materials—Slab Bonded, and Molded Urethane Foams. ASTM International: Novelty, OH, USA, 2017.
71. Tancogne-Dejean, T.; Mohr, D. Stiffness and specific energy absorption of additively-manufactured metallic BCC metamaterials composed of tapered beams. *Int. J. Mech. Sci.* **2018**, *141*, 101–116. [CrossRef]
72. Alhyari, O.; Newaz, G. Energy absorption in carbon fiber composites with holes under quasi-static loading. *C* **2021**, *7*, 16. [CrossRef]
73. Crocombe, A.D. *How to Tackle Non-Linear Finite Element Analysis*; NAFEMS: Knutsford, UK, 2001.
74. Nasim, M.; Hasan, M.J.; Galvanetto, U. Impact behavior of energy absorbing helmet liners with PA12 lattice structures: A computational study. *Int. J. Mech. Sci.* **2022**, *233*, 107673. [CrossRef]
75. Clauser, C.E.; Mc Conville, J.T.; Young, J.W. *Weight, Volume, and Center of Mass of Segments of the Human Body*; Report Number: NASA-CR-112672; NASA: Washington, DC, USA, 1969.
76. Frick, A.; Rochman, A. Characterization of TPU-elastomers by thermal analysis (DSC). *Polym. Test.* **2004**, *23*, 413–417. [CrossRef]
77. Que, Y.-H.; Shi, Y.; Liu, L.-Z.; Wang, Y.-X.; Wang, C.-C.; Zhang, H.-C.; Han, X.-Y. The Crystallisation, Microphase Separation and Mechanical Properties of the Mixture of Ether-Based TPU with Different Ester-Based TPUs. *Polymers* **2021**, *13*, 3475. [CrossRef]
78. Wegner, A.; Mielicki, C.; Grimm, T.; Gronhoff, B.; Witt, G.; Wortberg, J. Determination of robust material qualities and processing conditions for laser sintering of polyamide 12. *Polym. Eng. Sci.* **2014**, *54*, 1540–1554. [CrossRef]
79. Wang, X.-T.; Wang, B.; Li, X.-W.; Ma, L. Mechanical properties of 3D re-entrant auxetic cellular structures. *Int. J. Mech. Sci.* **2017**, *131*, 396–407. [CrossRef]
80. Cho, H.; Seo, D.; Kim, D. Mechanics of auxetic materials. In *Handbook of Mechanics of Materials*; Springer: Singapore, 2019; pp. 733–757.
81. Egan, P.F.; Khatri, N.R.; Parab, M.A.; Arefin, A.M.E. Mechanics of 3D-Printed Polymer Lattices with Varied Design and Processing Strategies. *Polymers* **2022**, *14*, 5515. [CrossRef] [PubMed]
82. Tancogne-Dejean, T.; Spierings, A.B.; Mohr, D. Additively-manufactured metallic micro-lattice materials for high specific energy absorption under static and dynamic loading. *Acta Mater.* **2016**, *116*, 14–28. [CrossRef]
83. Feng, J.; Fu, J.; Yao, X.; He, Y. Triply periodic minimal surface (TPMS) porous structures: From multi-scale design, precise additive manufacturing to multidisciplinary applications. *Int. J. Extreme Manuf.* **2022**, *4*, 022001. [CrossRef]
84. Mirhakimi, A.S.; Dubey, D.; Elbestawi, M.A. Laser powder bed fusion of bio-inspired metamaterials for energy absorption applications: A review. *J. Mater. Res. Technol.* **2024**, *31*, 2126–2155. [CrossRef]
85. Duncan, O.; Bailly, N.; Allen, T.; Petit, Y.; Wagnac, E.; Alderson, A. Effect of compressive strain rate on auxetic foam. *Appl. Sci.* **2021**, *11*, 1207. [CrossRef]
86. Duddleston, L. Polyamide (Nylon) 12 degradation during the selective laser sintering (SLS) process: A quantification for recycling optimization. Master's Thesis, University of Wisconsin–Madison, Madison, WI, USA, 2015.
87. Wudy, K.; Drummer, D.; Kuhnlein, F.; Drexler, M. Influence of degradation behavior of polyamide 12 powders in laser sintering process on produced parts. In *AIP Conference Proceedings*; American Institute of Physics: College Park, MD, USA, 2014.
88. Dotchev, K.; Yusoff, W. Recycling of polyamide 12 based powders in the laser sintering process. *Rapid Prototyp. J.* **2009**, *15*, 192–203. [CrossRef]
89. Pham, D.T.; Dotchev, K.D.; Yusoff, W.A.Y. Deterioration of polyamide powder properties in the laser sintering process. *Proc. Inst. Mech. Eng. Part C J. Mech. Eng. Sci.* **2008**, *222*, 2163–2176. [CrossRef]
90. Lin, T.A.; Lin, J.-H.; Bao, L. A study of reusability assessment and thermal behaviors for thermoplastic composite materials after melting process: Polypropylene/thermoplastic polyurethane blends. *J. Clean. Prod.* **2021**, *279*, 123473. [CrossRef]
91. Neff, C.; Trapuzzano, M.; Crane, N.B. Impact of vapor polishing on surface quality and mechanical properties of extruded ABS. *Rapid Prototyp. J.* **2018**, *24*, 501–508. [CrossRef]